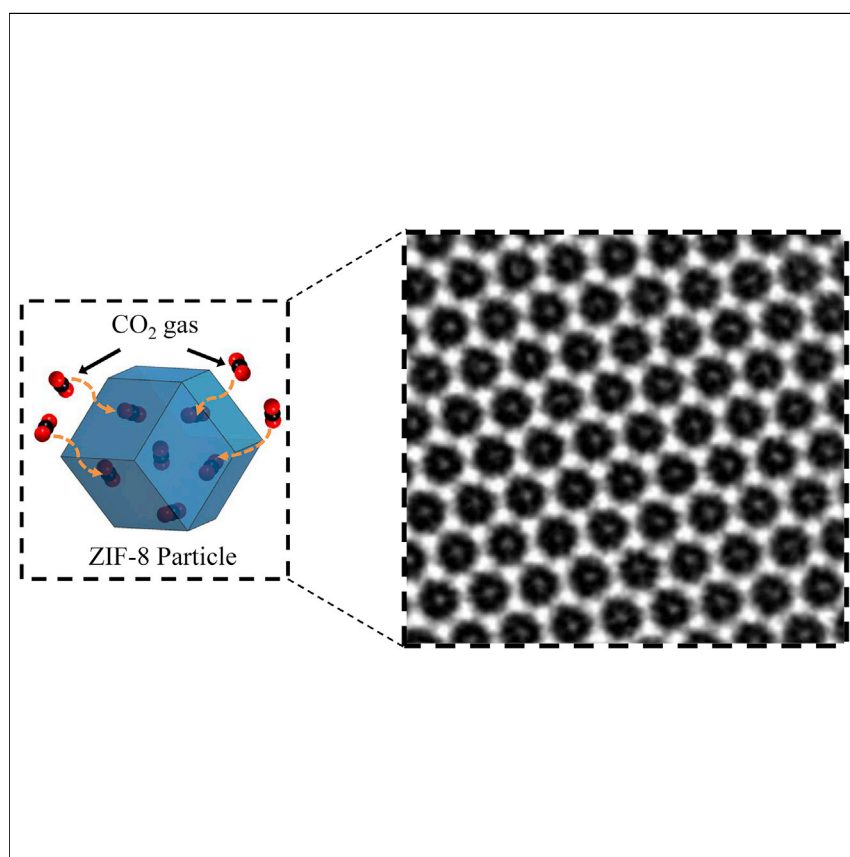


Article

Cryo-EM Structures of Atomic Surfaces and Host-Guest Chemistry in Metal-Organic Frameworks



Yuzhang Li, Kecheng Wang,
Weijiang Zhou, ..., Robert
Sinclair, Wah Chiu, Yi Cui

yicui@stanford.edu

HIGHLIGHTS

Cryo-EM preserves and stabilizes
host-guest interactions for
atomic-scale imaging

Guest molecules can be imaged
within frameworks for the first time

Upon CO₂ adsorption, the metal-
organic framework unit cell
expands by ~3%

Step-edge sites revealed at the
atomic surface provide hints at
growth mechanism

Metal-organic frameworks (MOFs) are a large class of highly porous materials whose chemistry and structure can be tuned for potential applications in gas storage, separations, and catalysis. Interactions between the host framework and guest molecule are central to these applications, but the local atomic structure and chemistry of such interactions is poorly understood. Using cryogenic electron microscopy, we reveal the structural changes of MOFs during guest intercalation and spatially resolve their binding sites within the framework.



Benchmark

First qualification/assessment of material
properties and/or performance

Li et al., Matter 1, 1–11
August 7, 2019 © 2019 Elsevier Inc.
<https://doi.org/10.1016/j.matt.2019.06.001>

Article

Cryo-EM Structures of Atomic Surfaces and Host-Guest Chemistry in Metal-Organic Frameworks

Yuzhang Li,^{1,8,9} Kecheng Wang,^{1,8} Weijiang Zhou,^{2,8} Yanbin Li,¹ Rafael Vila,¹ William Huang,¹ Hongxia Wang,¹ Guangxu Chen,¹ Gong-Her Wu,³ Yuchi Tsao,⁴ Hansen Wang,¹ Robert Sinclair,¹ Wah Chiu,^{2,3,5,6} and Yi Cui^{1,7,*}

SUMMARY

Host-guest interactions govern the chemistry of a broad range of functional materials, but direct imaging using conventional transmission electron microscopy has not been possible. This problem is exacerbated in metal-organic framework materials, which are easily damaged by the electron beam. Here, we use cryogenic electron microscopy (cryo-EM) to stabilize the host-guest structure and resolve the atomic surface of zeolitic imidazolate framework (ZIF-8) and its interaction with guest CO₂ molecules. We image step-edge sites on the ZIF-8 surface that provide insight to its growth behavior. Furthermore, we observe two distinct binding sites for CO₂ within the ZIF-8 pore, which are predicted by density functional theory to be energetically favorable. This CO₂ insertion induces an apparent ~3% lattice expansion along the <002> and <011> directions of the ZIF-8 unit cell. The ability to stabilize and preserve host-guest chemistry opens a rich materials space for scientific exploration and discovery using cryo-EM.

Metal-organic frameworks (MOFs) are a large class of highly porous materials^{1–3} whose chemistry and crystalline structure can be tuned for potential applications in gas storage,^{4–6} separations,⁷ and catalysis.⁸ Interactions between the host framework and guest molecule are central to such applications but are poorly understood at the molecular level. Although transmission electron microscopy (TEM) has been used to study the empty MOF framework,^{9–13} guest insertion within the MOFs could not be imaged. The weak bonding between the guest molecule and framework is easily damaged even under low electron doses.^{14,15} Furthermore, guest molecules are likely to desorb from MOF pores under the high-vacuum condition ($\sim 10^{-6}$ mbar) of the TEM at room temperature (Supplemental Experimental Procedures). Therefore, current studies rely on ensemble measurements using X-ray/neutron diffraction,^{16,17} nuclear magnetic resonance,¹⁸ or theoretical simulations.¹⁹ However, the structural information obtained by these methods is averaged over bulk particles. Direct observations of individual MOF particles and their interaction with guest species at high spatial resolution have not been possible.

Recently, cryogenic electron microscopy (cryo-EM) was shown to be a powerful tool beyond structural biology. For instance, reactive lithium battery materials have been successfully stabilized for imaging and spectroscopy.^{20–24} Such a cryogenic condition may also reduce radiation damage to the MOF framework (Supplemental Experimental Procedures). However, cryo-EM procedures developed for biological

Progress and Potential

Probing the local behavior in supramolecular chemistry with high spatial resolution has not yet been possible due to its sensitivity under electron irradiation. Here, we stabilize a beam-sensitive metal-organic framework (MOF) using cryogenic electron microscopy (cryo-EM) to produce the first atomic-resolution micrographs of host-guest interactions at the molecular level. These stark observations provide molecular-scale insight for particle growth and gas-adsorption kinetics. Specifically, we discover two preferred adsorption sites for CO₂, which induces a surprising ~3% lattice expansion for the MOF that was previously thought to be rigid. Furthermore, the atomic surface structure revealed by cryo-EM provides insight into MOF growth mechanisms. This specific example of CO₂ insertion into MOFs highlights the potential of cryo-EM in this large research field, opening up opportunities to study numerous host-guest interactions within a wide materials space.

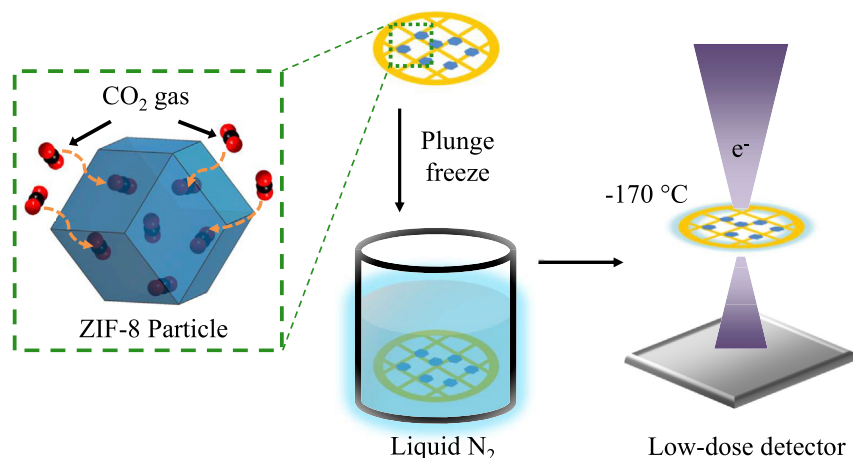


Figure 1. Preserving and Stabilizing Host-Guest Interactions Using Cryo-EM

Vacuum-dried ZIF-8 particles are exposed to CO₂ gas at ambient temperature and pressure after synthesis. In this environment, the particles are then plunge-frozen directly into liquid nitrogen to freeze in the host-guest structure and chemistry. Low-dose images are then recorded at cryogenic condition using a direct electron detector.

or battery materials are not necessarily compatible with MOFs. Here, we establish a new cryo-EM protocol to reveal atomic host-guest structures within MOFs, demonstrating that these entities, held together by weak interactions, can be preserved for high-resolution imaging under cryogenic conditions (Figure 1). As an example of this general approach, we investigate the surface structure of a zeolitic imidazolate framework (ZIF-8) and its host-guest chemistry with CO₂ molecules, with potential implications for both carbon capture and gas separations.²⁵

ZIF-8 is a body-centered cubic crystal that has a sodalite topology (space group $\bar{I}43m$). The ZIF-8 particles (~100 nm in diameter) synthesized in this study (Figure S2) are confirmed to be highly crystalline via X-ray diffraction (XRD; Figure S1). Diffraction contrast from the ZIF-8 particles observed in low-magnification TEM images (Figure 2A) further suggests a crystalline specimen. However, the bonding between the inorganic metal centers (Zn²⁺) and the organic linkers (2-methylimidazole) of the ZIF-8 framework is extremely sensitive to high electron doses. After exposure to ~50 e⁻/Å² at room temperature, the ZIF-8 particle quickly becomes amorphized, as indicated by both the high-resolution TEM (HRTEM) image (Figure 2B) and its fast Fourier transform (FFT; Figure 2B, inset). Indeed, previous studies^{12,13} have shown that MOF materials quickly lose their crystallinity with an accumulated electron dose of only ~10–20 e⁻/Å², with ZIF-8 becoming completely amorphous after 70 e⁻/Å² at room temperature. Consequently, any existing host-guest structure would be difficult to identify from the amorphized particle. To overcome these challenges, we established a flash-freezing protocol modified from cryo-EM methodologies used in structural biology²⁶ to preserve the MOFs at their operating environment (e.g., empty or filled) for high-resolution imaging. First, the as-synthesized ZIF-8 particles were dispersed onto a carbon support TEM grid and vacuum-dried to remove all solvent from the ZIF-8 pore space. Samples were then directly plunged into liquid nitrogen while maintaining vacuum or kept in a 1-bar pressure CO₂ environment (Figure 1A and Supplemental Experimental Procedures). This freezing process prevents any air exposure and kinetically inhibits CO₂ desorption from the ZIF-8, preserving the host-guest interactions that were present at room temperature.

¹Department of Materials Science and Engineering, Stanford University, Stanford, CA 94305, USA

²Biophysics Program, School of Medicine, Stanford University, Stanford, CA 94305, USA

³Department of Bioengineering, Stanford University, Stanford, CA 94305, USA

⁴Department of Chemistry, Stanford University, Stanford, CA 94305, USA

⁵Department of Microbiology and Immunology, Stanford University School of Medicine, Stanford, CA 94305, USA

⁶Division of CryoEM and Bioimaging, SSRL, SLAC National Accelerator Laboratory, Menlo Park, CA 94025, USA

⁷Stanford Institute for Materials and Energy Sciences, SLAC National Accelerator Laboratory, Menlo Park, CA 94025, USA

⁸These authors contributed equally

⁹Lead Contact

*Correspondence: yicui@stanford.edu
<https://doi.org/10.1016/j.matt.2019.06.001>

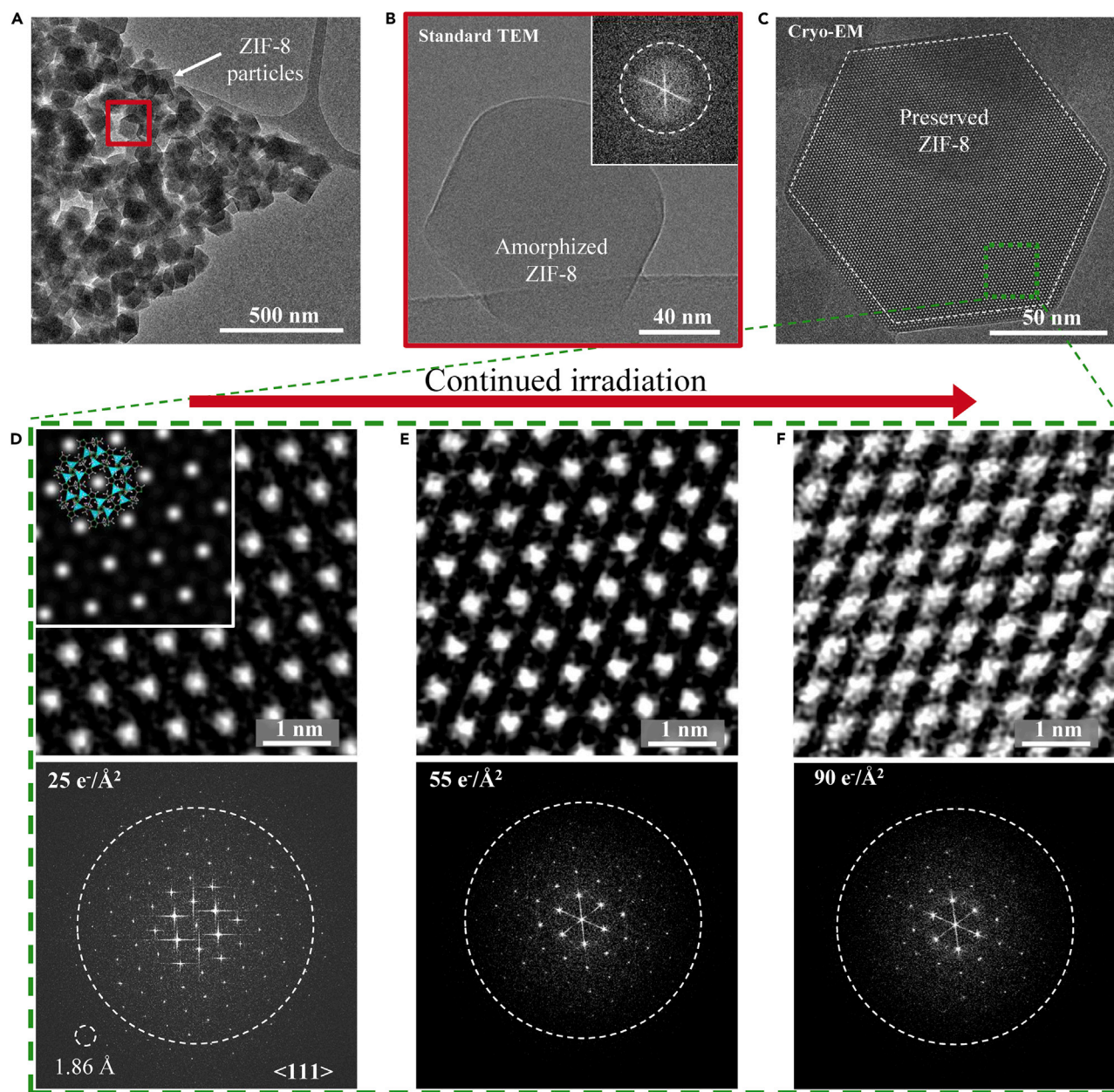


Figure 2. Electron Irradiation of ZIF-8 at Cryogenic Temperatures

(A) TEM image of ZIF-8 particles taken at room temperature with electron dose rate $2 \text{ e}^-/\text{\AA}^2/\text{s}$ for $\sim 1 \text{ s}$. Diffraction contrast suggests the sample is crystalline.

(B) HRTEM image of red boxed region from (A). After accumulated electron dose of $\sim 50 \text{ e}^-/\text{\AA}^2$, ZIF-8 becomes completely amorphous. Inset: corresponding FFT showing no crystallinity in the sample.

(C) Cryo-EM image of ZIF-8 (outlined by dashed white line) taken along the $\langle 111 \rangle$ direction at -170°C with electron dose rate of $\sim 4.5 \text{ e}^-/\text{\AA}^2/\text{s}$ for 1.5 s. At 225-nm underfocus, bright spots in the ZIF-8 lattice correspond to empty pore space.

(D–F) Magnified images of green boxed region from (C) exposed to electron doses of $25 \text{ e}^-/\text{\AA}^2$ (D), $50 \text{ e}^-/\text{\AA}^2$ (E), and $90 \text{ e}^-/\text{\AA}^2$ (F) with corresponding FFT pattern below. The dashed circle on the FFT represents an information transfer of 2.5 \AA . Information transfer of 1.86 \AA is possible, as indicated by the reflection circled in (D). Inset of (D): the ZIF-8 atomic structure is overlaid onto the simulated TEM image, which is calculated using 225-nm underfocus and 100-nm sample thickness. The simulated image matches reasonably well with the experimental cryo-EM image.

Cryogenic temperature is known to reduce radiation damage induced by the electron beam.^{14,27} In our cryo-EM imaging experiment, we keep the specimen at -170°C and expose it to different cumulative electron doses to determine its

radiation damage sensitivity (Figure S7). We use a magnification corresponding to a pixel size of 0.68 by 0.68 Å to facilitate imaging at atomic resolution. In addition, a direct-detection electron-counting camera has a high quantum efficiency to enable acquisition of images with high signal-to-noise at all frequencies and a high frame rate to allow recording of multiple frames per specimen area followed by subsequent frame alignment to minimize beam-induced drift.²⁸

Figure 2C is a typical cryo-EM image of a ZIF-8 particle that was held under vacuum before flash-freezing. When viewed along the $\langle 111 \rangle$ zone axis, the ZIF-8 rhombic dodecahedral particle is hexagonal (dashed white lines) with well-defined $\{011\}$ edge planes joined by sharp vertices (Figure S3). Furthermore, the crystalline structure of the ZIF-8 particle is clearly preserved. Under low-dose and low-temperature conditions, the ZIF-8 structure shows structure information down to 1.86 Å as evidenced by the FFT of this image (Figure 2D, bottom), exceeding previously reported resolutions of ZIF-8. A simulated TEM image (Figure 2D, inset) also shows good agreement with the raw image. Even after exposure to $25 \text{ e}^-/\text{Å}^2$ that would ordinarily result in significant damage to the framework, ZIF-8 remains pristine at low temperatures (Figure 2D). When the number of frames taken and the cumulative exposure are increased (Figures 2E and 2F), ZIF-8 shows only partial loss of crystallinity after $90 \text{ e}^-/\text{Å}^2$ at low temperature, while the same specimen becomes fully amorphous after exposure of $50 \text{ e}^-/\text{Å}^2$ at room temperature (Figure 2B). Quantitatively, the plot of normalized intensity in the FFT as a function of cumulative electron exposure (Figure S7) demonstrates that high-resolution information (3 Å) is still retained after $90 \text{ e}^-/\text{Å}^2$. These experiments and the corresponding raw, unprocessed images (Figure S5) establish the increased stability of ZIF-8 using cryo-EM, allowing further exploration into its surface atomic structure and host-guest chemistry.

The atomic surfaces of materials often provide insight into their growth mechanism. In particular, the shape and size uniformity of ZIF-8 particles has been attributed to the formation of surface steps.^{29,30} Unfortunately, surface structures and their possible defects are more sensitive than the bulk to the electron beam, making atomic-resolution imaging difficult even at low electron doses.¹² To preserve and study such surface structures immediately after growth, the as-synthesized ZIF-8 particles were flash-frozen and imaged without vacuum-drying (Supplemental Experimental Procedures). Using a $\sim 7 \text{ e}^-/\text{Å}^2$ cumulative electron dose, we have made a number of structural feature observations previously not seen at room temperature. Figure 3A is a denoised³¹ cryo-EM image of ZIF-8 after synthesis, which appears to be free of defects in the bulk and directly matches the ZIF-8 crystal structure projected along the $\langle 111 \rangle$ direction. In brief, denoising was done by subtracting amorphous background signal from the Fourier transform to improve the visibility of crystalline components. At an overfocus of 250 nm, the hexagonal columns of bright contrast correspond to the “Zn clusters” centers of the framework, as confirmed by TEM simulation (Supplemental Experimental Procedures). Here, we denote a “Zn cluster” as the collection of Zn metal centers and connecting ligands that constitute one of the six ZIF-8 hexagonal vertices visible along the $\langle 111 \rangle$ projection (Figure 3B, inset). With cryo-EM, it is now possible to resolve atomically sharp surfaces of ZIF-8, demonstrating the striking resolution and stability afforded by this technique. We find that the exposed $\{011\}$ ZIF-8 surfaces terminate with doubly coordinated Zn clusters, indicating that Zn clusters on the surface are joined with two other clusters. By reducing the number of dangling ligands, this doubly coordinated Zn cluster conformation exposes a thermodynamically stable termination surface. Interestingly, these surfaces are not atomically pristine. Instead,

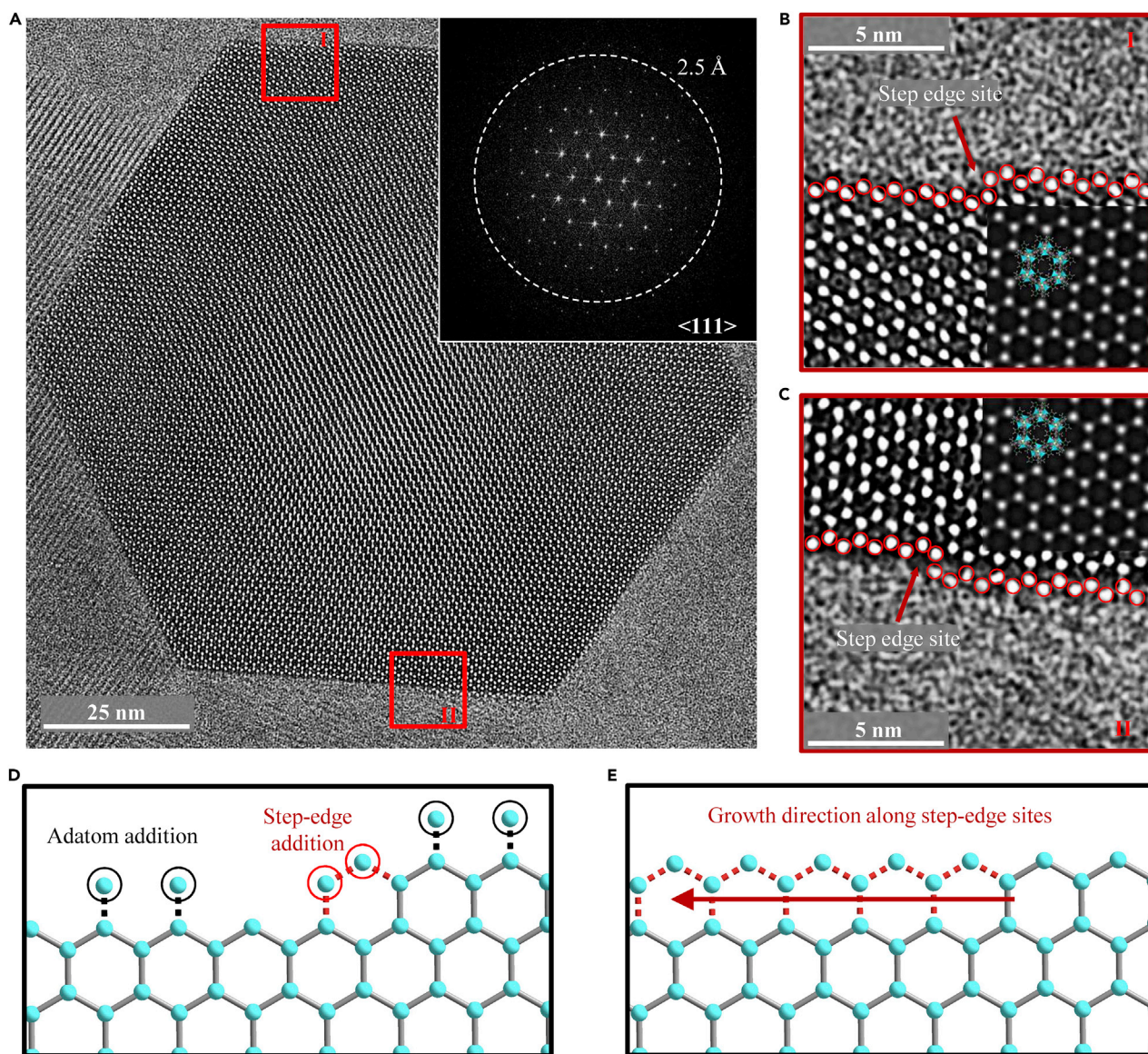


Figure 3. Atomic Surface and Step-Edge Sites of ZIF-8 Particles

(A) Denoised cryo-EM image of ZIF-8 after synthesis (not vacuum-dried) taken at 250-nm overfocus with electron dose rate of $\sim 4.5 \text{ e}^-/\text{\AA}^2/\text{s}$ for 1.5 s. Bright spots correspond to Zn clusters. Inset: corresponding FFT pattern. White dashed circle represents information transfer of 2.5 Å.

(B and C) Magnified images of region I (B) and region II (C) boxed in red from (A). The ZIF-8 atomic structure is overlaid onto a simulated TEM image in the second inset, which is calculated using 250-nm overfocus and 100-nm sample thickness. The simulated TEM image matches well with the experimental cryo-EM image. The Zn clusters on the surface are double-coordinated and are outlined in red circles. A step-edge site is observed in both (B) and (C), indicated by the red arrow.

(D) Schematic of possible surface additions of Zn clusters during ZIF-8 growth. Whereas adatom addition (circled in black) would result in single-coordinated Zn clusters, addition at the step-edge site (circled in red) would result in double-coordinated Zn clusters.

(E) Schematic of ZIF-8 growth initiated at the step-edge site, which is thermodynamically more favorable.

step-edge defects are clearly present in regions I (Figure 3B) and II (Figure 3C), which may play an important role in the growth mechanism of ZIF-8. Particle growth of ZIF-8 requires the addition of Zn clusters to the exposed surface. This process is not random. Whereas any two adatom clusters of Zn at a surface site would only be singly coordinated, addition of any two Zn clusters at a step-edge site would enable double coordination of both (Figure 3D). Therefore, it is thermodynamically

favorable for ZIF-8 growth to initiate at step-edge sites rather than surface sites (Figure 3E), which is consistent with our observations (Figures S4 and S6). Finally, bright intensity is visible inside the 6-ring channels of ZIF-8 (Figures 3B and 3C), which may come from the solvent molecule within the pore that exists during synthesis (i.e., acetone or methanol). Along with this observation, the low vapor pressure of guest molecules at cryogenic temperature ($\sim 10^{-10}$ mbar for CO_2) suggests that host-guest interactions can be stabilized for imaging using cryo-EM (Supplemental Experimental Procedures).

Raw, unprocessed cryo-EM images of an empty (Figure 4A) and CO_2 -filled (Figure 4D) ZIF-8 particle appear to be very similar when taken at an underfocus of 225 nm. To make a fair comparison between these two images, we correct the “contrast inversion” (Supplemental Experimental Procedures) introduced by the contrast transfer function (CTF) of the objective lens.³² Here, the weak-phase object approximation applies to sample thicknesses up to ~ 100 nm owing to the low density of ZIF-8, which reduces its effective scattering thickness.¹³ This standard image-processing procedure (Supplemental Experimental Procedures) generates CTF-corrected images of empty ZIF-8 (Figure 4B) and CO_2 -filled ZIF-8 (Figure 4E) in which the regions of bright intensity represent mass density,^{33,34} making interpretation of such CTF-corrected images more straightforward. Zn clusters at the unit cell vertices appear as bright dots, forming the expected hexagonal honeycomb lattice along the $\langle 111 \rangle$ projection in both the empty and filled ZIF-8 particle. Within the ZIF-8 pore, distinguishing features between the empty and filled state are quite dramatic. Whereas density is absent within the center pore space of empty ZIF-8 unit cells, bright contrast is clearly visible in the middle of the CO_2 -filled ZIF-8 pore. This suggests that CO_2 adsorption is centered within the 6-ring window along the $\langle 111 \rangle$ direction. Indeed, TEM simulations (Figures S8 and S9) and density functional theory (DFT) calculations of favorable CO_2 binding sites in ZIF-8 support our observations.³⁵ Using such calculations, we simulate the structure of a ZIF-8 unit cell with the DFT-optimized binding location of CO_2 molecules (simplified as red spheres) projected along the $\langle 111 \rangle$ direction. The simulated structure (Figure 4G) matches well with the CTF-corrected cryo-EM image (Figure 4E), providing strong evidence that CO_2 molecules are successfully preserved within the framework at cryogenic conditions and can be directly imaged using cryo-EM.

Close inspection of a single ZIF-8 unit cell reveals several key features of the host material during guest insertion. In the empty ZIF-8 pore (Figure 4C), there are three areas of density (circled in blue) just inside the edges of the unit cell. This contrast likely comes from the three organic imidazolate linkers that protrude into the pore space, forming the 6-ring windows that connect each individual pore. Interestingly, these moieties are not observed in ZIF-8 unit cells after CO_2 loading (Figure 4F), suggesting that the imidazolate linkers can rotate out of view to open the narrow 6-ring window (3.4 Å) for CO_2 (3.3 Å kinetic diameter) adsorption and diffusion throughout the framework. These results support previous descriptions of a “gate-opening” phenomenon in ZIF-8, which explains how molecules larger than the 6-ring window (e.g., N_2 3.6 Å kinetic diameter) can be accommodated into ZIF-8 pores via linker rotation.^{36–39} Although it is generally accepted that flexibility of the 6-ring windows occurs at various loading conditions, the ZIF-8 pore cavity itself is largely thought to remain rigid upon CO_2 insertion at ambient pressures. Surprisingly, we discover a 3% expansion of the $\langle 011 \rangle$ lattice repeat during CO_2 loading at atmospheric pressure. Figure 4H plots the integrated pixel intensities for the empty and CO_2 -filled ZIF-8 unit cells along the

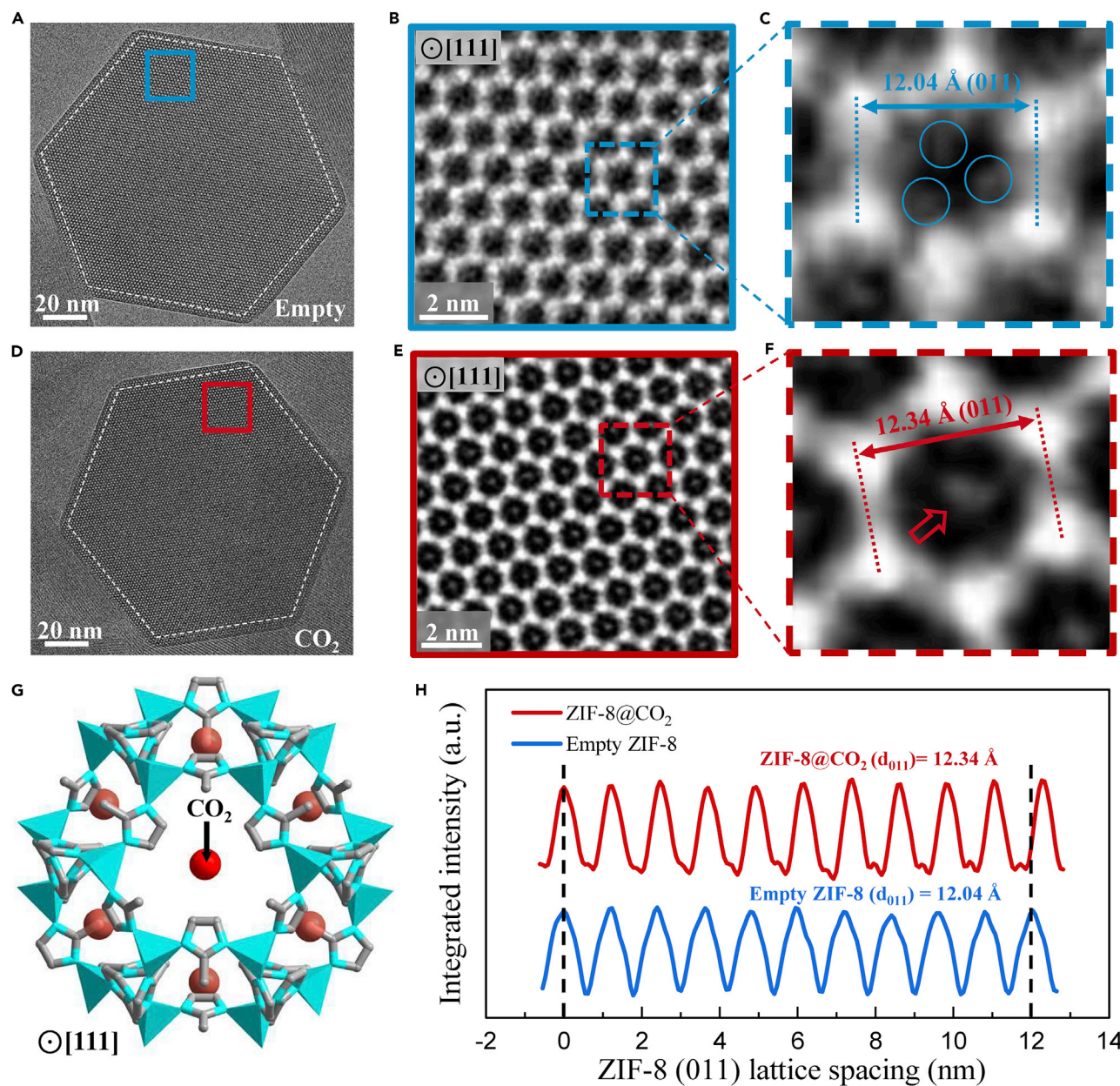


Figure 4. Host-Guest Structures within ZIF-8 Viewed along $\langle 111 \rangle$ Projection

(A) Cryo-EM image of vacuum-dried, empty ZIF-8 (outlined by white dashed lines) taken with electron dose rate of $\sim 4.5 \text{ e}^-/\text{\AA}^2/\text{s}$ for 1.5 s along the $\langle 111 \rangle$ projection.

(B) CTF-corrected denoised image of blue boxed region from (A). Bright regions correspond to mass density.

(C) Magnified image of a single ZIF-8 unit cell from (B). Density (circled in blue) near the interior edge of the unit cell may correspond to the organic imidazolite linkers.

(D) Cryo-EM image of CO_2 -filled ZIF-8 particle (outlined by white dashed lines) taken with electron dose rate of $\sim 4.5 \text{ e}^-/\text{\AA}^2/\text{s}$ for 1.5 s along the $\langle 111 \rangle$ projection.

(E) CTF-corrected denoised image of red boxed region from (D). Bright regions correspond to mass density. Contrast in the center of the 6-ring window is clearly observed for multiple unit cells.

(F) Magnified image of a single ZIF-8 unit cell from (E). Density at the center of the unit cell (indicated by red arrow) likely corresponds to CO_2 adsorbed within ZIF-8.

(G) Simulated structure of ZIF-8 with DFT-predicted binding site of CO_2 (simplified as red spheres) along the $\langle 111 \rangle$ projection. This is consistent with the experimental cryo-EM image from (F).

(H) Integrated intensity of ZIF-8 plotted over 10 unit cells along the $\langle 011 \rangle$ direction, indicating a 3% lattice expansion when CO_2 is introduced to ZIF-8.

$\langle 011 \rangle$ direction. The $\langle 011 \rangle$ lattice spacing for the empty ZIF-8 averaged over 10 unit cells is measured to be 12.04 Å (Figure S10), which matches well with the experimental value of 12.03 Å from XRD measurement.³⁶ The precision in this TEM lattice measurement is approximately 0.07 Å (Supplemental Experimental Procedures). After CO₂ loading, the ZIF-8 $\langle 011 \rangle$ lattice expands to 12.34 Å (Figure S11). Although lattice expansions of this magnitude (~3%) are possible for ZIF-8,⁴⁰ they have predominantly been observed at high-pressure loadings (~10⁴ bar) of non-interacting gas molecules (e.g., N₂, O₂, Ar). However, the CO₂ still induces a similar unit cell expansion at much lower pressure (~1 bar CO₂ loading) in our experiments. This observation implies a strong interaction between CO₂ and the ZIF-8 framework, which further suggests that ZIF-8 might be a promising carbon capture material.

To reinforce our results, it is important to investigate the host-guest structures along more than one zone axis. Projected in the $\langle 001 \rangle$ direction, the rhombic dodecahedral ZIF-8 particle appears as a square (Figures 5A and 5D). With CTF correction to address the contrast inversion issue mentioned above, the cryo-EM images of empty (Figure 5B) and CO₂-filled (Figure 5E) ZIF-8 can be more easily interpreted. Contrast is strongest for the Zn clusters, which are located at the bright square spots. These clusters are connected by the imidazolate linkers that are visible as lines of white contrast. When viewed along the $\langle 001 \rangle$ direction (Figure 5C), ZIF-8 displays two structurally distinct pore cavities: one is located at the vertex of the Zn cluster (circled in green) and the second is adjacent to the square edge of the Zn cluster (boxed in orange). Both cavities do not appear to contain any density in the empty ZIF-8 (Figure 5C). Upon CO₂ adsorption, bright contrast can be observed in the center of the 4-ring window (Figure 5F). Interestingly, this appears only in the pore cavity located at the vertex of the Zn cluster and not the cavity at the Zn cluster edge. Although adsorption at the center of these particular 4-ring windows is different from the CO₂-binding location observed along the $\langle 111 \rangle$ direction, DFT calculations show that CO₂ binding centered around the 4-ring window is also energetically favorable.³⁵ The simulated ZIF-8 structure with the predicted CO₂ adsorption site (Figure 5G) closely resembles the cryo-EM image (Figure 5F), indicating that more than one adsorption site exists. Furthermore, the lattice expansion observed for the $\langle 011 \rangle$ direction is also present along the $\langle 002 \rangle$ direction (Figure 5H). Whereas an 8.56-Å $\langle 002 \rangle$ lattice spacing is measured for the empty ZIF-8 (Figure S12), the $\langle 002 \rangle$ expands 3% to 8.78 Å after CO₂ insertion (Figure S13). The similar unit cell expansion and additional adsorption sites revealed here demonstrate the increased information gained by simply observing the particles along different crystallographic directions. To identify possible adsorption sites beyond the two observed here, a full tomographic tilt series of a single ZIF-8 particle can now be enabled by the additional stability afforded by cryo-EM.

Our work here demonstrates the powerful utility for cryo-EM to preserve and image atomic MOF surface structures and guest molecules within its pore cavities. We revealed that ZIF-8 growth likely initiates at a step-edge surface site and discovered structural changes in ZIF-8 during CO₂ insertion. This study opens opportunities to further investigate such host-guest interactions and develop a complete picture of MOF adsorption kinetics at the single-particle level. Using cryo-EM, the many applications of different MOFs with distinct guest molecules can be probed at the atomic level. New discoveries and findings will provide insight into their fundamental operation and shape future designs of these tunable materials.

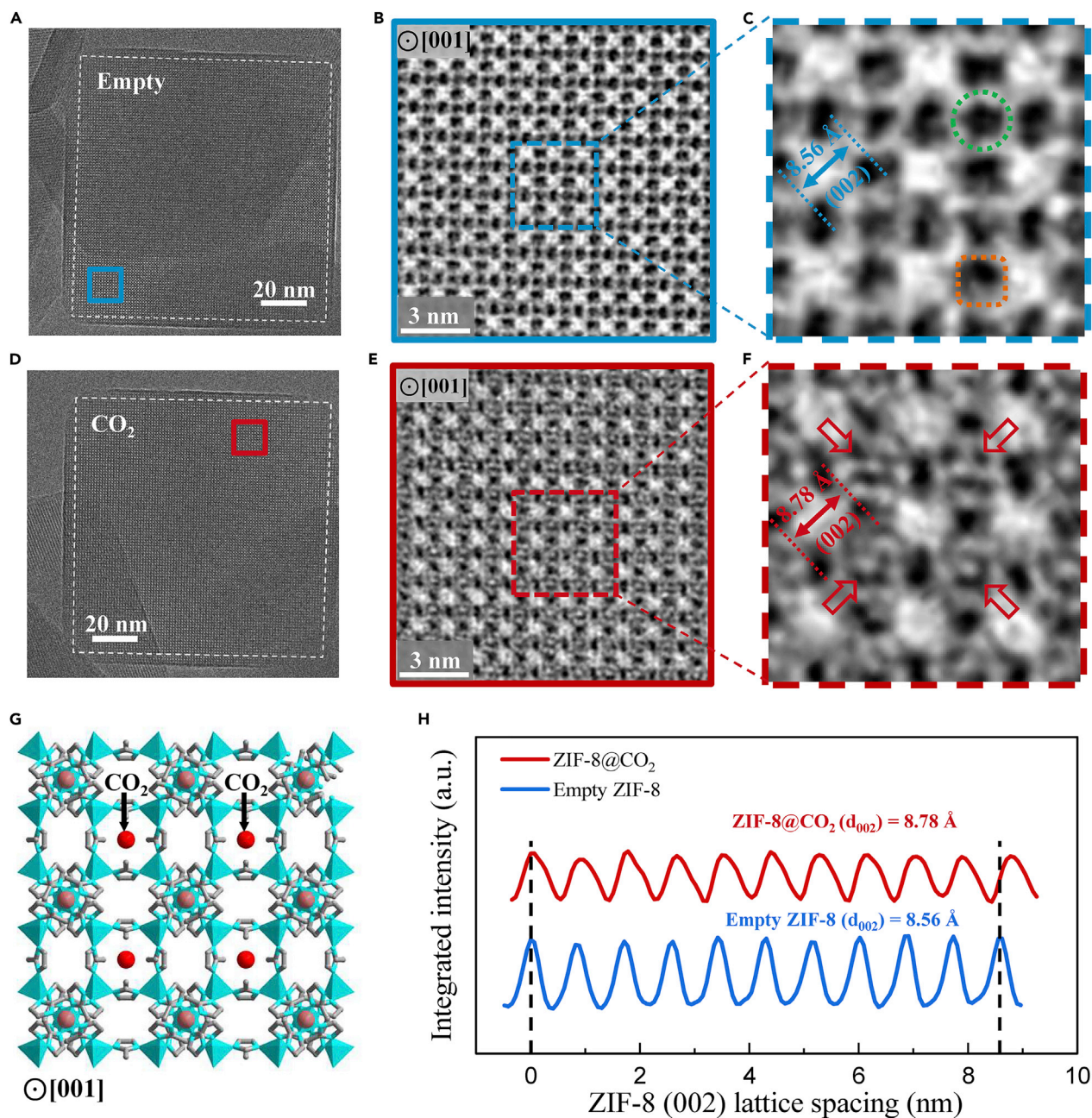


Figure 5. Host-Guest Structures within ZIF-8 Viewed along $\langle 001 \rangle$ Projection

(A) Cryo-EM image of vacuum-dried, empty ZIF-8 (outlined by white dashed lines) taken with electron dose rate of $\sim 4.5 \text{ e}^-/\text{\AA}^2/\text{s}$ for 1.5 s along the $\langle 001 \rangle$ projection. (B) CTF-corrected denoised image of blue boxed region from (A). Bright regions correspond to mass density. (C) Magnified image of ZIF-8 unit cells in blue box from (B). Green circle indicates pore cavity at the vertices of the Zn clusters. Orange square indicates pore cavity at the edges of the Zn clusters. (D) Cryo-EM image of CO_2 -filled ZIF-8 particle (outlined by white dashed lines) taken with electron dose rate of $\sim 4.5 \text{ e}^-/\text{\AA}^2/\text{s}$ for 1.5 s along the $\langle 001 \rangle$ projection. (E) CTF-corrected denoised image of red boxed region from (D). Bright regions correspond to mass density. Contrast near the center of the 4-ring window is clearly observed for multiple unit cells. (F) Magnified image of ZIF-8 unit cells in red box from (E). Density near the center of the unit cell (indicated by red arrows) likely corresponds to CO_2 adsorbed within ZIF-8. Note that only the pore cavity at the vertices of the 4-ring window contains the density in the center. (G) Simulated structure of ZIF-8 with DFT-predicted binding site of CO_2 (simplified as red spheres) along the $\langle 001 \rangle$ projection. This is consistent with the experimental cryo-EM image from (F). (H) Integrated intensity of ZIF-8 plotted over 10 unit cells along the $\langle 002 \rangle$ direction, indicating a 3% lattice expansion when CO_2 is introduced to ZIF-8.

SUPPLEMENTAL INFORMATION

Supplemental Information can be found online at <https://doi.org/10.1016/j.matt.2019.06.001>.

ACKNOWLEDGMENTS

The authors thank Dave Bushnell and Dong-Hua Chen for training at the Stanford-SLAC cryo-EM facilities. Y.L. acknowledges the Intelligence Community Fellowship for funding. Part of this work was performed at the Stanford Nano Shared Facilities, supported by the National Science Foundation under award ECCS-1542152. R.S. acknowledges support from the National Institutes of Health (NIH) under grant no. U54 CA199075. W.C. acknowledges support by the NIH under grant nos. P41GM103832 and S10OD021600. Y.C. acknowledges support from the Department of Energy, Office of Basic Energy Sciences, Division of Materials Sciences and Engineering, under contract DE-AC02-76SF00515.

AUTHOR CONTRIBUTIONS

Yuzhang Li and Y.C. conceived the idea and designed the experiments. Yuzhang Li, Yanbin Li, H.W., and G.C. established the cryo-plunging methodologies. Yuzhang Li, K.W., and Y.T. synthesized the ZIF-8 particles. Yuzhang Li, Yanbin Li, G.-H.W., and W.Z. performed the cryo-EM experiments. W.Z. processed the CTF-corrected images. R.V. simulated the TEM images according to experimental imaging conditions. W.H. and H.W. conducted other EM characterizations at room temperature. Yuzhang Li, K.W., W.Z., R.S., W.C., and Y.C. interpreted the results and co-wrote the paper. All authors discussed the results and commented on the manuscript.

DECLARATION OF INTERESTS

The authors declare no competing financial interests.

Received: May 3, 2019

Revised: May 23, 2019

Accepted: May 31, 2019

Published: June 26, 2019

REFERENCES

- Li, H., Eddaoudi, M., O'Keeffe, M., and Yaghi, O.M. (1999). Design and synthesis of an exceptionally stable and highly porous metal-organic framework. *Nature* *402*, 276.
- Yaghi, O.M., O'Keeffe, M., Ockwig, N.W., Chae, H.K., Eddaoudi, M., and Kim, J. (2003). Reticular synthesis and the design of new materials. *Nature* *423*, 705.
- Furukawa, H., Cordova, K.E., O'Keeffe, M., and Yaghi, O.M. (2013). The chemistry and applications of metal-organic frameworks. *Science* *341*, 1230444.
- Eddaoudi, M., Kim, J., Rosi, N., Vodak, D., Wachter, J., O'Keefe, M., and Yaghi, O.M. (2002). Systematic design of pore size and functionality in isoreticular MOFs and their application in methane storage. *Science* *295*, 469–472.
- Rosi, N.L., Eckert, J., Eddaoudi, M., Vodak, D., Kim, J., O'Keefe, M., and Yaghi, O.M. (2003). Hydrogen storage in microporous metal-organic frameworks. *Science* *300*, 1127–1129.
- Sumida, K., Rogow, D.L., Mason, J.A., McDonald, T.M., Bloch, E.D., Herm, Z.R., Bae, T.-H., and Long, J.R. (2011). Carbon dioxide capture in metal-organic frameworks. *Chem. Rev.* *112*, 724–781.
- Li, J.-R., Kuppler, R.J., and Zhou, H.-C. (2009). Selective gas adsorption and separation in metal-organic frameworks. *Chem. Soc. Rev.* *38*, 1477–1504.
- Lee, J., Farha, O.K., Roberts, J., Scheidt, K.A., Nguyen, S.T., and Hupp, J.T. (2009). Metal-organic framework materials as catalysts. *Chem. Soc. Rev.* *38*, 1450–1459.
- Lebedev, O.I., Millange, F., Serre, C., Van Tendeloo, G., and Férey, G. (2005). First direct imaging of giant pores of the metal-organic framework MIL-101. *Chem. Mater.* *17*, 6525–6527.
- Cravillon, J., Münzer, S., Lohmeier, S.J., Feldhoff, A., Huber, K., and Wiebcke, M. (2009). Rapid room-temperature synthesis and characterization of nanocrystals of a prototypical zeolitic imidazolate framework. *Chem. Mater.* *21*, 1410–1412.
- Wiktor, C., Turner, S., Zacher, D., Fischer, R.A., and Van Tendeloo, G. (2012). Imaging of intact MOF-5 nanocrystals by advanced TEM at liquid nitrogen temperature. *Microporous Mesoporous Mater.* *162*, 131–135.
- Zhu, Y., Ciston, J., Zheng, B., Miao, X., Czarnik, C., Pan, Y., Sougrat, R., Lai, Z., Hsiung, C.E., Yao, K., et al. (2017). Unravelling surface and interfacial structures of a metal-organic framework by transmission electron microscopy. *Nat. Mater.* *16*, 532.
- Zhang, D., Zhu, Y., Liu, L., Ying, X., Hsiung, C.E., Sougrat, R., Li, K., and Han, Y. (2018). Atomic-resolution transmission electron microscopy of electron beam-sensitive crystalline materials. *Science* *359*, 675–679.
- Egerton, R.F., Li, P., and Malac, M. (2004). Radiation damage in the TEM and SEM. *Micron* *35*, 399–409.

15. Wiktor, C., Meledina, M., Turner, S., Lebedev, O.I., and Fischer, R.A. (2017). Transmission electron microscopy on metal-organic frameworks—a review. *J. Mater. Chem. A* **5**, 14969–14989.
16. Rowsell, J.L.C., Spencer, E.C., Eckert, J., Howard, J.A.K., and Yaghi, O.M. (2005). Gas adsorption sites in a large-pore metal-organic framework. *Science* **309**, 1350–1354.
17. Easun, T.L., Moreau, F., Yan, Y., Yang, S., and Schröder, M. (2017). Structural and dynamic studies of substrate binding in porous metal-organic frameworks. *Chem. Soc. Rev.* **46**, 239–274.
18. Witherspoon, V.J., Xu, J., and Reimer, J.A. (2018). Solid-state NMR investigations of carbon dioxide gas in metal-organic frameworks: insights into molecular motion and adsorptive behavior. *Chem. Rev.* **118**, 10033–10048.
19. Landers, J., Gor, G.Y., and Neimark, A.V. (2013). Density functional theory methods for characterization of porous materials. *Colloids Surfaces A Physicochem. Eng. Asp.* **437**, 3–32.
20. Li, Y., Pei, A., Yan, K., Sun, Y., Wu, C.L., Joubert, L.M., Chin, R., Koh, A.L., Yu, Y., Perrino, J., et al. (2017). Atomic structure of sensitive battery materials and interfaces revealed by cryo-electron microscopy. *Science* **358**, 506–510.
21. Wang, X., Zhang, M., Alvarado, J., Wang, S., Sina, M., Lu, B., Bouwer, J., Xu, W., Xiao, J., Zhang, J.-G., et al. (2017). New insights on the structure of electrochemically deposited lithium metal and its solid electrolyte interphases via cryogenic TEM. *Nano Lett.* **17**, 7606–7612.
22. Zachman, M.J., Tu, Z., Choudhury, S., Archer, L.A., and Kourkoutis, L.F. (2018). Cryo-STEM mapping of solid-liquid interfaces and dendrites in lithium-metal batteries. *Nature* **560**, 345.
23. Li, Y., Huang, W., Li, Y., Pei, A., Boyle, D., and Cui, Y. (2018). Correlating structure and function of battery interphases at atomic resolution using cryo-electron microscopy. *Joule*. <https://doi.org/10.1016/j.joule.2018.08.004>.
24. Li, Y., Li, Y., and Cui, Y. (2018). Catalyst: how cryo-EM shapes the development of next-generation batteries. *Chem* **4**, 2250–2252.
25. Park, K.S., Ni, Z., Côté, A.P., Choi, J.Y., Huang, R., Uribe-Romo, F.J., Chae, H.K., O’Keeffe, M., and Yaghi, O.M. (2006). Exceptional chemical and thermal stability of zeolitic imidazolate frameworks. *Proc. Natl. Acad. Sci. U S A* **103**, 10186–10191.
26. Chiu, W. (1986). Electron microscopy of frozen, hydrated biological specimens. *Annu. Rev. Biophys. Chem.* **15**, 237–257.
27. Egerton, R.F. (2012). Mechanisms of radiation damage in beam-sensitive specimens, for TEM accelerating voltages between 10 and 300 kV. *Microsc. Res. Tech.* **75**, 1550–1556.
28. Li, X., Mooney, P., Zheng, S., Booth, C.R., Braunfeld, M.B., Gubbens, S., Agard, D.A., and Cheng, Y. (2013). Electron counting and beam-induced motion correction enable near-atomic-resolution single-particle cryo-EM. *Nat. Methods* **10**, 584.
29. Moh, P.Y., Cubillas, P., Anderson, M.W., and Attfield, M.P. (2011). Revelation of the molecular assembly of the nanoporous metal organic framework ZIF-8. *J. Am. Chem. Soc.* **133**, 13304–13307.
30. Wagia, R., Strashnov, I., Anderson, M.W., and Attfield, M.P. (2018). Insight and control of the crystal growth of zeolitic imidazolate framework ZIF-67 by atomic force microscopy and mass spectrometry. *Cryst. Growth Des.* **18**, 695–700.
31. Kilaas, R. (1998). Optimal and near-optimal filters in high-resolution electron microscopy. *J. Microsc.* **190**, 45–51.
32. Zou, X., Hovmöller, S., and Oleynikov, P. (2011). *Electron Crystallography: Electron Microscopy and Electron Diffraction*, **16** (Oxford University Press).
33. Rohou, A., and Grigorieff, N. (2015). CTFFIND4: fast and accurate defocus estimation from electron micrographs. *J. Struct. Biol.* **192**, 216–221.
34. Zhang, K. (2016). Gctf: real-time CTF determination and correction. *J. Struct. Biol.* **193**, 1–12.
35. Fischer, M., and Bell, R.G. (2014). Interaction of hydrogen and carbon dioxide with sod-type zeolitic imidazolate frameworks: a periodic DFT-D study. *CrystEngComm* **16**, 1934–1949.
36. Fairen-Jimenez, D., Moggach, S.A., Wharmby, M.T., Wright, P.A., Parsons, S., and Düren, T. (2011). Opening the gate: framework flexibility in ZIF-8 explored by experiments and simulations. *J. Am. Chem. Soc.* **133**, 8900–8902.
37. Zhang, C., Moggach, S.A., Wharmby, M.T., Wright, P.A., Parsons, S., and Düren, T. (2012). Unexpected molecular sieving properties of zeolitic imidazolate framework-8. *J. Phys. Chem. Lett.* **3**, 2130–2134.
38. Haldoupis, E., Watanabe, T., Nair, S., and Sholl, D.S. (2012). Quantifying large effects of framework flexibility on diffusion in MOFs: CH₄ and CO₂ in ZIF-8. *ChemPhysChem* **13**, 3449–3452.
39. Zhang, K., Lively, R.P., Zhang, C., Chance, R.R., Koros, W., Sholl, D.S., and Nair, S. (2013). Exploring the framework hydrophobicity and flexibility of ZIF-8: from biofuel recovery to hydrocarbon separations. *J. Phys. Chem. Lett.* **4**, 3618–3622.
40. Hobday, C.L., Woodall, C.H., Lennox, M.J., Frost, M., Kamenev, K., Düren, T., Morrison, C.A., and Moggach, S.A. (2018). Understanding the adsorption process in ZIF-8 using high pressure crystallography and computational modelling. *Nat. Commun.* **9**, 1429.

Matter, Volume 1

Supplemental Information

Cryo-EM Structures of Atomic Surfaces

and Host-Guest Chemistry

in Metal-Organic Frameworks

Yuzhang Li, Kecheng Wang, Weijiang Zhou, Yanbin Li, Rafael Vila, William Huang, Hongxia Wang, Guangxu Chen, Gong-Her Wu, Yuchi Tsao, Hansen Wang, Robert Sinclair, Wah Chiu, and Yi Cui

Materials and Methods

ZIF-8 synthesis

Rhombic dodecahedral ZIF-8 nanoparticles on the order of ~100 nm were synthesized following previously established protocols¹. Two solutions were used in the synthesis: (1) 3.39g of imidazole dissolved in 125 mL of 99.8% anhydrous methanol and (2) 3.08g of $\text{Zn}(\text{NO}_3)_2 \cdot 6\text{H}_2\text{O}$ dissolved in 125 mL 99.8% anhydrous methanol. The entirety of solution 2 consisting of the Zn precursor was added dropwise into solution 1 (imidazole) with vigorous stirring. The mixed solution was stirred for 2 hr at ambient conditions. The white precipitates (ZIF-8 nanocrystals) were collected by centrifugation and washed three times with methanol to remove the impurities. The samples were then suspended in acetone until the cryo-transfer procedure (below). All chemicals were purchased from Sigma Aldrich and used without further purification unless otherwise mentioned.

Cryo-transfer procedure

Empty ZIF-8: After synthesis, ZIF-8 particles suspended in acetone were dropcast onto a Cu TEM grid with lacey C support (Ted Pella). The samples were then placed into a sealed vial with a rubber cap. A sharp needle was inserted into the rubber cap and a vacuum was created using a Schlenk line. The sample was then dried under vacuum at 60 °C for 4 hrs. After drying, the vial (still under vacuum) was then immediately plunged into liquid nitrogen and physically crushed with pliers, exposing the TEM grid to the cryogen. The sample was then transferred into the TEM column while immersed in liquid nitrogen using an autoloader (Thermo Fisher).

CO₂-filled ZIF-8: Sample preparation proceeds exactly as the empty ZIF-8 until after vacuum-drying, during which 99.999% ultrahigh purity CO₂ gas (Praxair) was fed through the needle for 5 min at 50 sccm. A second hole in the rubber cap was punctured during CO₂ insertion to avoid pressure build up. After 5 min, the vial (still under CO₂ flow) was then immediately plunged into

liquid nitrogen and physically crushed with pliers, exposing the TEM grid to the cryogen. The sample was then transferred into the TEM column while immersed in liquid nitrogen using an autoloader (Thermo Fisher).

As-synthesized ZIF-8: After synthesis, ZIF-8 particles suspended in acetone were dropcast onto a Cu TEM grid with lacey C support (Ted Pella) and dried for 2 hrs at ambient conditions. After drying, the TEM grid was then immediately plunged into liquid nitrogen. The sample was then transferred into the TEM column while immersed in liquid nitrogen using an autoloader (Thermo Fisher).

Instrumentation

All room temperature TEM characterizations were carried out using an FEI Titan 80-300 environmental (scanning) transmission electron microscope (E(S)TEM) operated at 300 kV. The microscope was equipped with an aberration corrector in the image-forming (objective) lens, which was tuned before each sample analysis. During the TEM image acquisition, the corresponding electron dose flux (measured in units of number of electrons per square Angström per second, $e^- \text{Å}^{-2} \cdot \text{s}^{-1}$) was also recorded. This parameter had been calibrated for the instrument using an analytical TEM holder with a Faraday cup. All cryo-EM experiments were performed on a Thermo Fisher Titan Krios G2 TEM operated at 300 kV and equipped with an autoloading mechanism. Cryo-EM images were acquired by a Gatan K2 direct-detection camera in the electron-counting mode with the Dose-Fractionation function. Lattice spacings of ZIF-8 unit cells were analyzed using DigitalMicrograph (Gatan) software. Powder X-ray diffraction was carried out with a BRUKER D8-Focus Bragg-Brentano X-ray Powder Diffractometer equipped with a Cu sealed tube ($\lambda = 1.54178 \text{ Å}$) operating at 40 kV and 40 mA. SEM characterizations were carried out using a FEI Magellan 400 XHR SEM at room temperature.

Cryo-EM imaging conditions

Well-aligned samples were identified among randomly oriented ZIF-8 particles by their strong diffraction contrast at zone-axis using low magnifications of $\sim 1,000$ ($< 0.1 \text{ e}^-/\text{\AA}^2/\text{s}$). Considering the radiation sensitivity of the material, continuous exposure to adjust objective lens focus is impractical. Several short exposure (0.2s) single-frame shots were taken to estimate the defocus and make it as close as possible to Scherzer defocus (90 nm for this microscope with a spherical aberration coefficient of 2.7 mm). Then, cryo-EM images were taken at a nominal magnification of 37,000 with a pixel size of 0.6864 \AA by 0.6864 \AA and an electron dose rate of $4.14 \text{ e}^-/\text{\AA}^2/\text{s}$ ($1.82 \text{ e}^-/\text{\AA}^2/\text{pixel}$). The true magnification was calibrated using a standard Au cross grating TEM grid. Each image was recorded for 1.5s using a Dose-Fractionation of 0.1s/frame, resulting in 15 frames per image that was later motion-corrected. The defocus was estimated by reading the output of the TEM user interface after resetting the defocus to zero at focus (minimum contrast).

Image processing

We follow the most recent data processing protocols established for cryo-EM to make post-image analysis more generalizable and accessible. First, dose fraction frames were motion-corrected by MotionCor2² to correct beam-induced movements. The conditions of defocus and astigmatism were determined by CTFFIND4³ and GCTF⁴ followed by a manual inspection. The motion-corrected images were then phase flipped by a set of MRC programs⁵ used to handle 2D protein crystal cryo-EM images in traditional electron crystallography. The procedures described above can be done either separately or combined in a modern software package FOCUS⁶ with a user-friendly GUI. The amplitude correction is not included in our CTF correction to avoid artifacts.

Finally, the CTF-corrected images were denoised by as Average Background Subtraction Filter (ABSF) and a Wiener filter, which are commonly used in HRTEM to produce clear images⁷. Both filters were applied to every image to avoid potential artifacts introduced by a specific filter.

HRTEM image simulation

Cryo-EM images at high-resolutions were simulated using the multi-slice method with Dirac-Fock ionic scattering potentials⁸ employed in the Quantitative TEM/STEM (QSTEM) simulation software (<http://www.qstem.org>). Appropriate imaging conditions and aberration coefficients were selected according to the experimental parameters. Specifically, a 300 kV accelerating voltage, convergence semi-angle of 0.15 mrad, spherical aberration (C_s) value of 2.7 mm, and a focal spread of 5 nm. Specimen thickness was selected as 100 nm, corresponding to the approximate diameters observed for the ZIF-8 nanocrystals. The pixel size of the simulated HRTEM image was adjusted to 0.68 Å according to the experimentally acquired image.

Lattice spacing analysis

The lattice spacing of the ZIF-8 unit cells is measured using DigitalMicrograph software along both the $\langle 002 \rangle$ and $\langle 011 \rangle$ directions. First, the direction of interest ($\langle 002 \rangle$ or $\langle 011 \rangle$) is identified by inspection. Then, the pixel intensities perpendicular to this direction are summed over 100 pixels (~ 6.8 nm). These integrated pixel intensities are then plotted vs. lattice distance for ~ 10 ZIF-8 unit cells. Peak maxima are observed to be correct within one pixel (0.68 Å). Thus, the uncertainty of the measurements over 10 unit cells is ~ 0.07 Å. In addition to measuring the intensity plots of the HRTEM image, we also measured the lattice spacings using the intensity from the FFT, which was calibrated using a standard Au cross grating TEM grid. These

measurements from the FFT match well with the measurements from the HRTEM image. An example of this procedure is shown in figs. S11-S18.

Supplementary Text

TEM radiation damage mechanisms

Metal-organic frameworks contain a hybrid of inorganic and organic materials. In particular, ZIF-8 is an electrically insulating MOF material, making it susceptible to radiation damage by both radiolysis and knock-on displacement⁹. Since MOF crystallinity is dependent on the metal-ligand bonds that can easily be damaged by radiolysis, amorphization will occur rapidly even with relatively low electron doses ($\sim 50 \text{ e}^-/\text{\AA}^2$). Using cryo-EM at low temperatures, we significantly reduce radiolysis damage without needing to lower the accelerating voltage¹⁰. This allows us to capture images with high resolution and a longer penetration depth. However, knock-on damage will still degrade the sample, given enough electron exposure. Thus, the stability at cryogenic temperatures, as is the case for structural biology, does not last indefinitely.

Stabilization of CO₂ molecules at cryogenic temperatures

As mentioned in the main text, it is likely that CO₂ molecules will desorb from the ZIF-8 framework under high vacuum inside the TEM ($\sim 10^{-6}$ mbar) at room temperature. This is because the vapor pressure of CO₂ at room temperature (~ 298 K) is extremely high (~ 60 bar). At cryogenic temperatures (~ 80 K), the vapor pressure of CO₂ can be estimated by extensions to Antoine's equation. From tabulated parameters of Antoine's equation for CO₂ at low temperatures¹¹ and direct experimental measurements¹², the vapor pressure of CO₂ at 80 K is within $\sim 10^{-11} - 10^{-9}$ mbar. Assuming a TEM column pressure of 10^{-6} mbar with atmospheric composition (~ 500 ppm CO₂), the partial pressure of CO₂ inside the TEM is approximately $\sim 10^{-9}$ mbar. Since the

equilibrium vapor pressure of CO₂ at cryogenic temperatures is on the order of the partial pressure of CO₂ already present within the TEM, desorption from the framework is both kinetically and thermodynamically reduced or inhibited.

Distinction between “denoising” and CTF-correction”

The Wiener filter used in our manuscript is used to deconvolute the CTF in the presence of noise⁷. After correction of “contrast inversion”, we further used this Wiener filter to improve the visibility of crystalline regions in the HRTEM images and reduce the noise generated by the background amorphous carbon. Additionally, for clarity, we have added the raw images into the supplemental materials to demonstrate the high data quality in fig. S6-S7.

Supplementary Figures

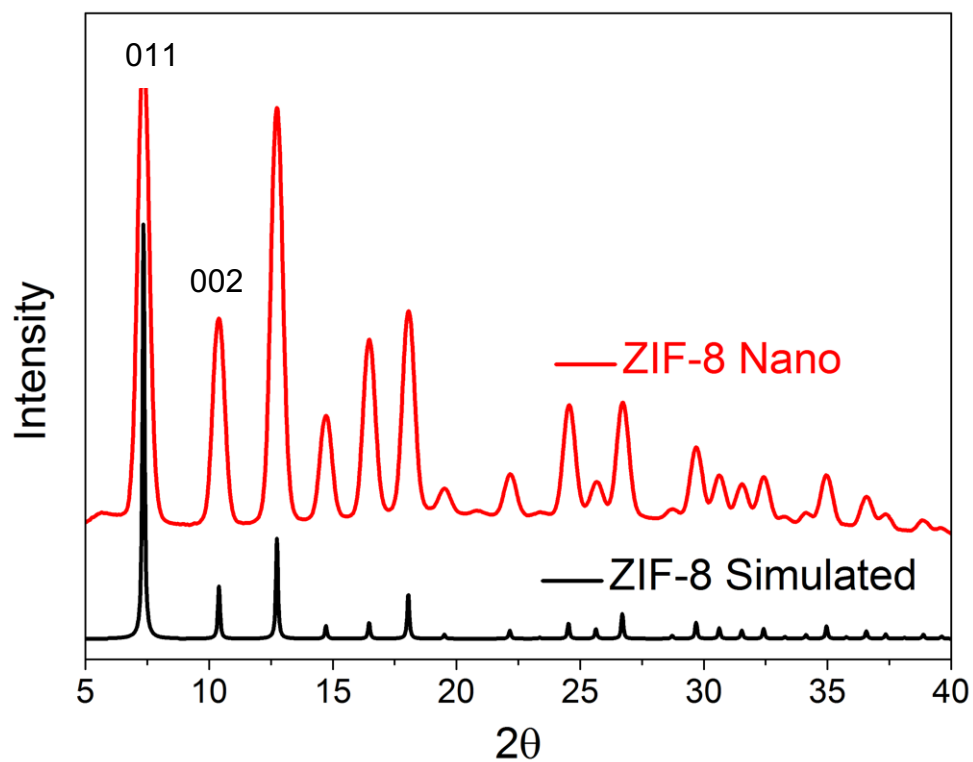


Fig. S1. Powder XRD profiles. Simulated (black) and experimental (red) profiles of the body-centered cubic ZIF-8 nanocrystals are plotted, demonstrating that the sample is crystalline and matches the simulated structure.

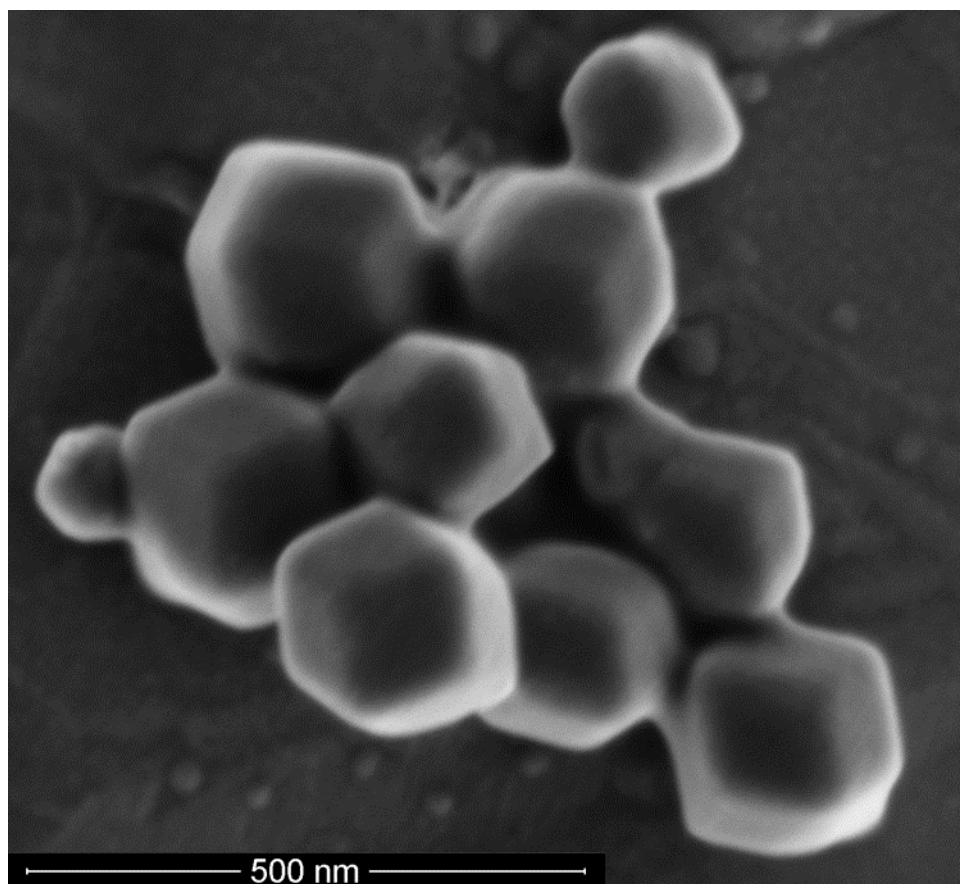


Fig. S2. SEM of ZIF-8 particles. The rhombic dodecahedral shape of the ZIF-8 nanocrystals can be observed, with clear faceting at the particle faces. Particle sizes are on the order of 100 nm in thickness. Secondary electron SEM images taken at 1 kV.

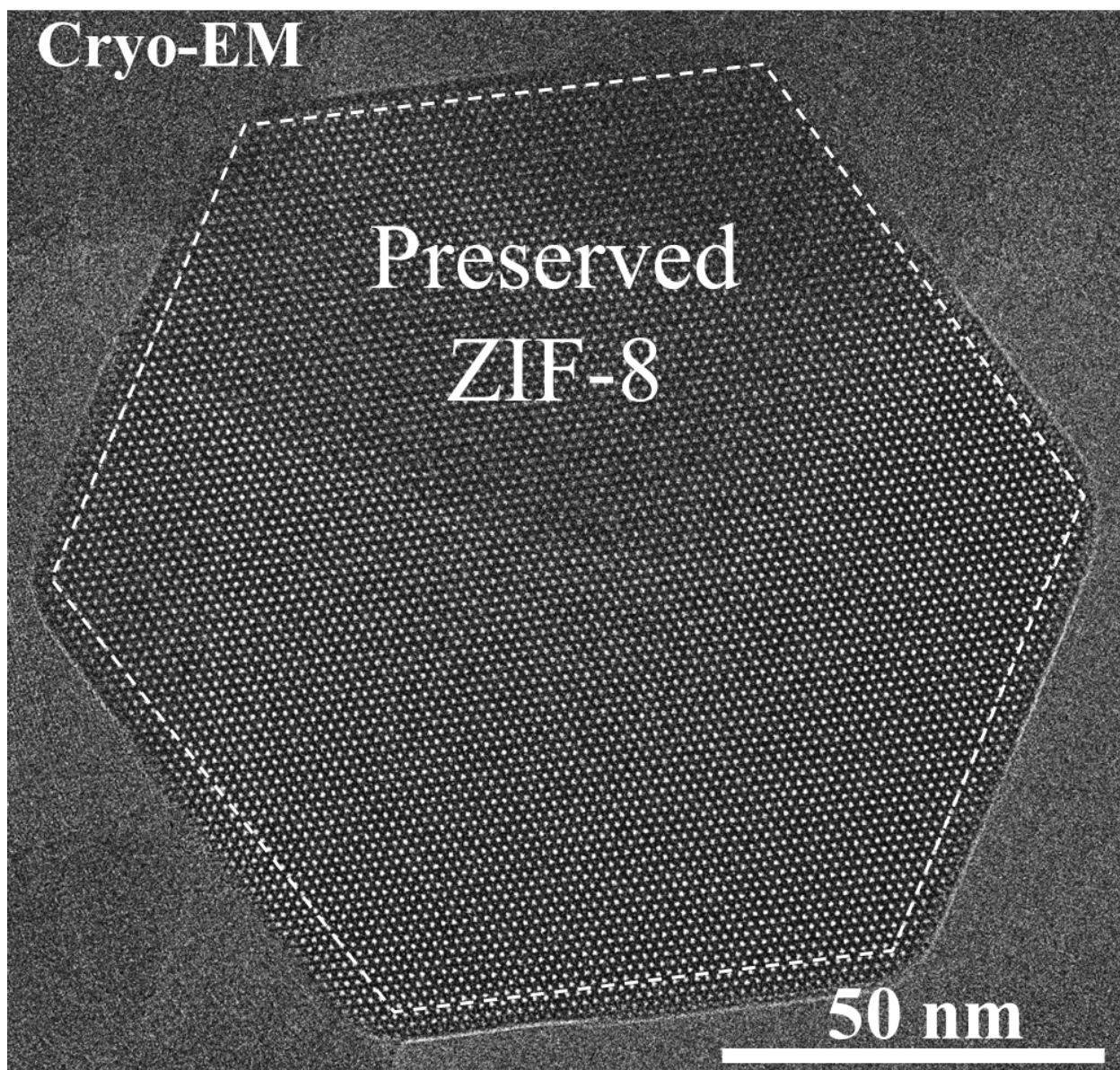


Fig. S3. Magnified image of Fig. 2c. Drift-corrected cryo-EM image of ZIF-8 taken at 225 nm underfocus along the $\langle 111 \rangle$ zone axis. Bright spots indicate pore space within the 6-ring windows. Facets exposed are the $\{011\}$ family of planes.

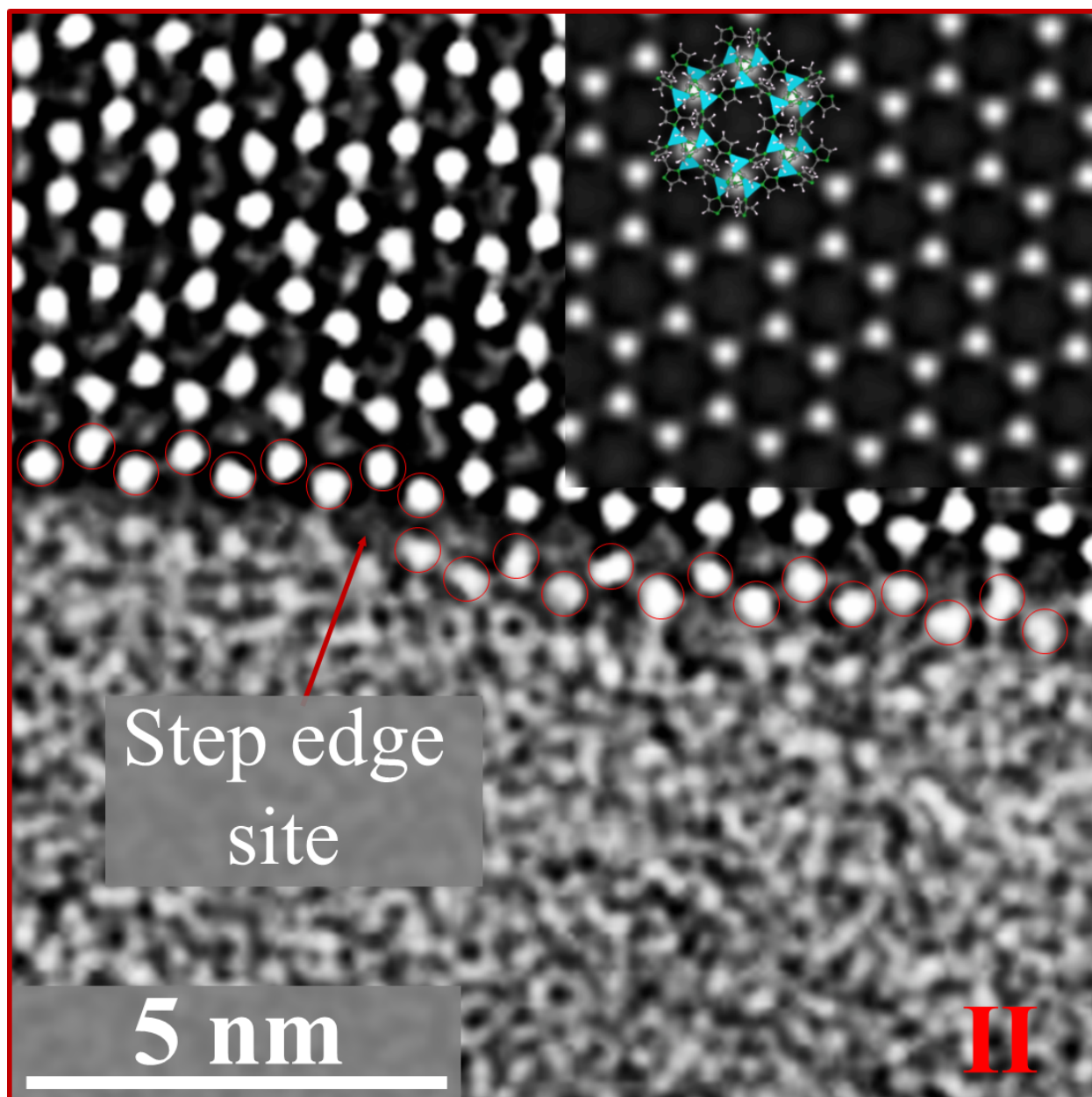


Fig. S4. Magnified image of Fig. 3c. Bright spots correspond to Zn metal clusters at overfocus of 250 nm. The simulated ZIF-8 structure (inset) matches reasonably well with the drift-corrected cryo-EM image. Step edge site is clearly visible on the surface.

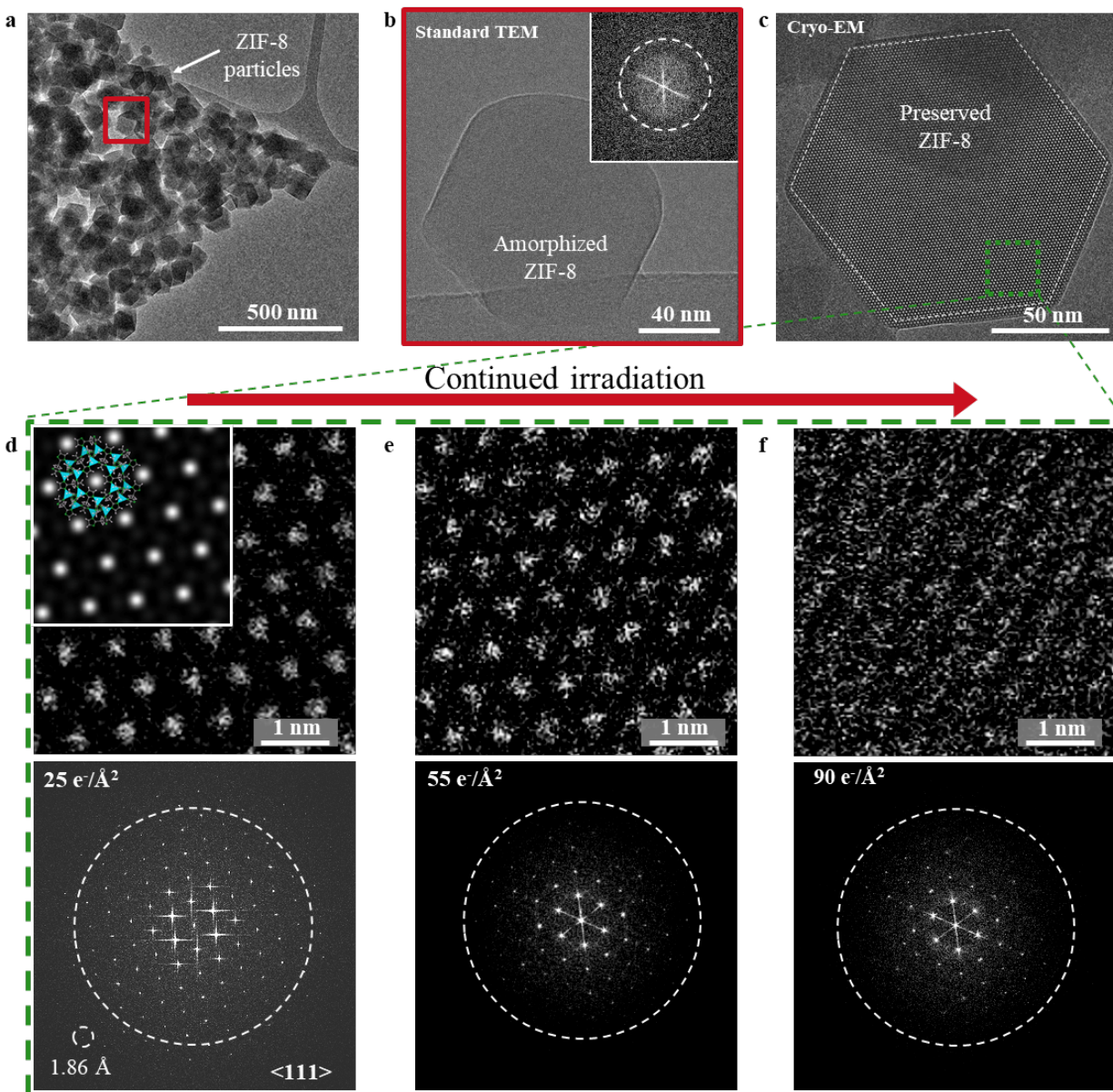


Fig. S5. Raw, unfiltered, uncorrected images of Fig 2. Fig. S6c-S6f here are the raw images without any post-processing (i.e. denoising or CTF-correction) corresponding to Fig. 2c-2f in the main text. The inner ring of FFT spots corresponds to the $\{011\}$ reflections.

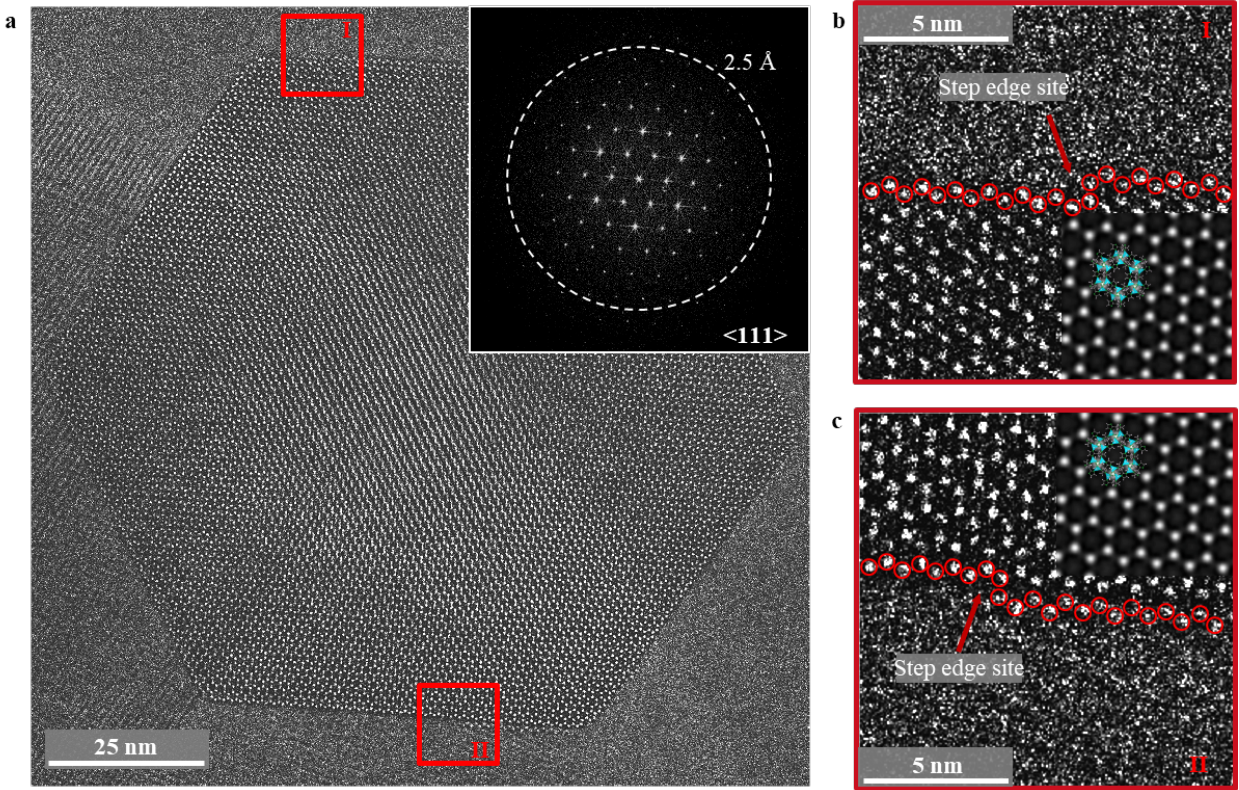


Fig. S6. Raw, unfiltered, uncorrected images of Fig 3. Fig. S7a-S7c here are the raw images without any post-processing (i.e. denoising or CTF-correction) corresponding to Fig. 3a-3c in the main text.

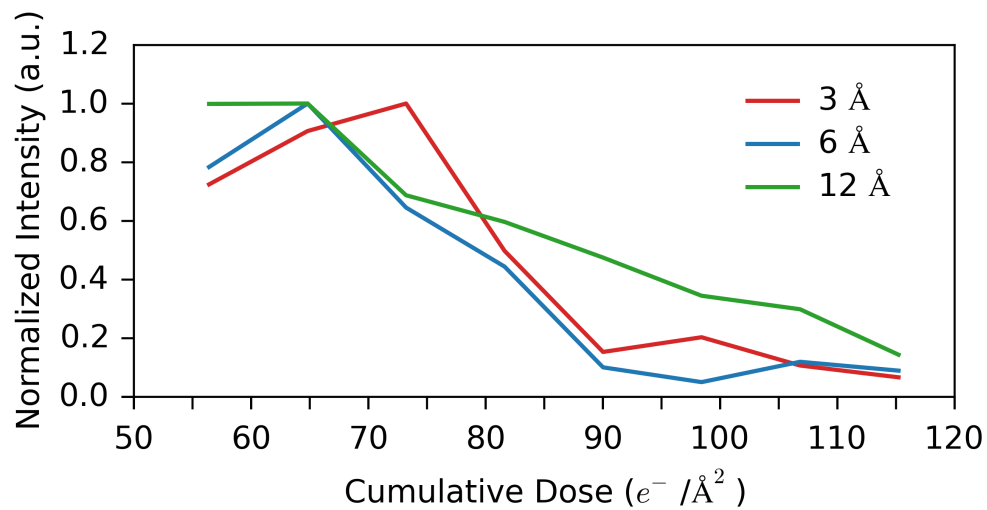


Fig. S7. Quantitative characterization of irradiation tests. Plot of the normalized intensity of 3 selected regions from the FFT's in Fig. 2d-2f in the main text after exposure to various cumulative exposures at liquid nitrogen temperature. For example, the red curve (3 Å) represents the region in the FFT that corresponds to 3 Å resolution.

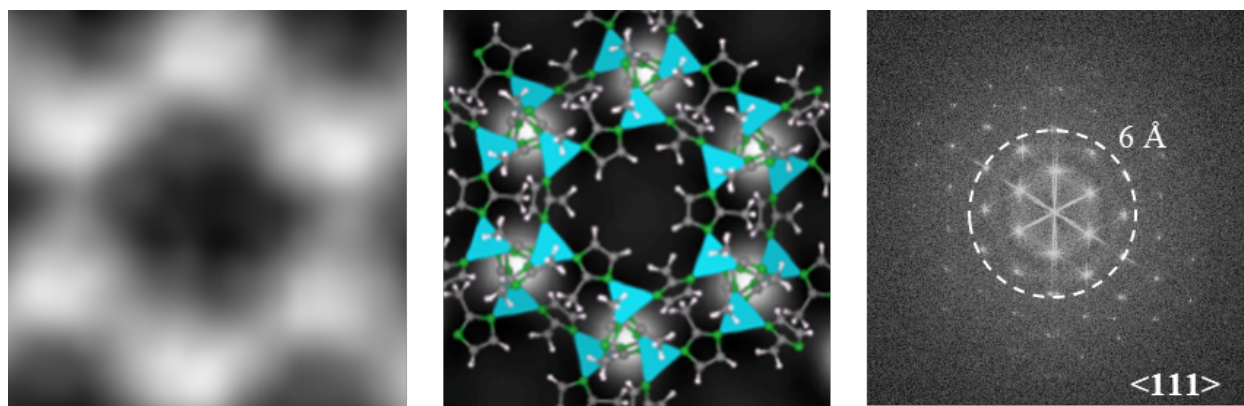


Fig. S8. HRTEM simulation of empty ZIF-8. (Left) Experimental filtered image (obtained by masking out all spots in the FFT using the array-mask function from DigitalMicrograph and then using those spots to generate an inverse FFT) of empty ZIF-8 unit cell. (Middle) Simulated image of an empty ZIF-8 unit cell superimposed on the projected structure that matches reasonably well with the experimental image. (Right) Corresponding FFT of the ZIF-8 particle from Fig. 4a after exposure to $\sim 100 \text{ e}/\text{\AA}^2$.



Fig. S9. HRTEM simulation of CO₂-filled ZIF-8. (Left) Denoised CTF-corrected cryo-EM image of CO₂-filled ZIF-8 unit cell. (Middle) Experimental filtered image (obtained by masking out all spots in the FFT using the array-mask function from DigitalMicrograph and then using those spots to generate an inverse FFT) of CO₂-filled ZIF-8 unit cell. (Right) Simulated image of CO₂-filled ZIF-8 unit cell that matches reasonably well with the experimental image.

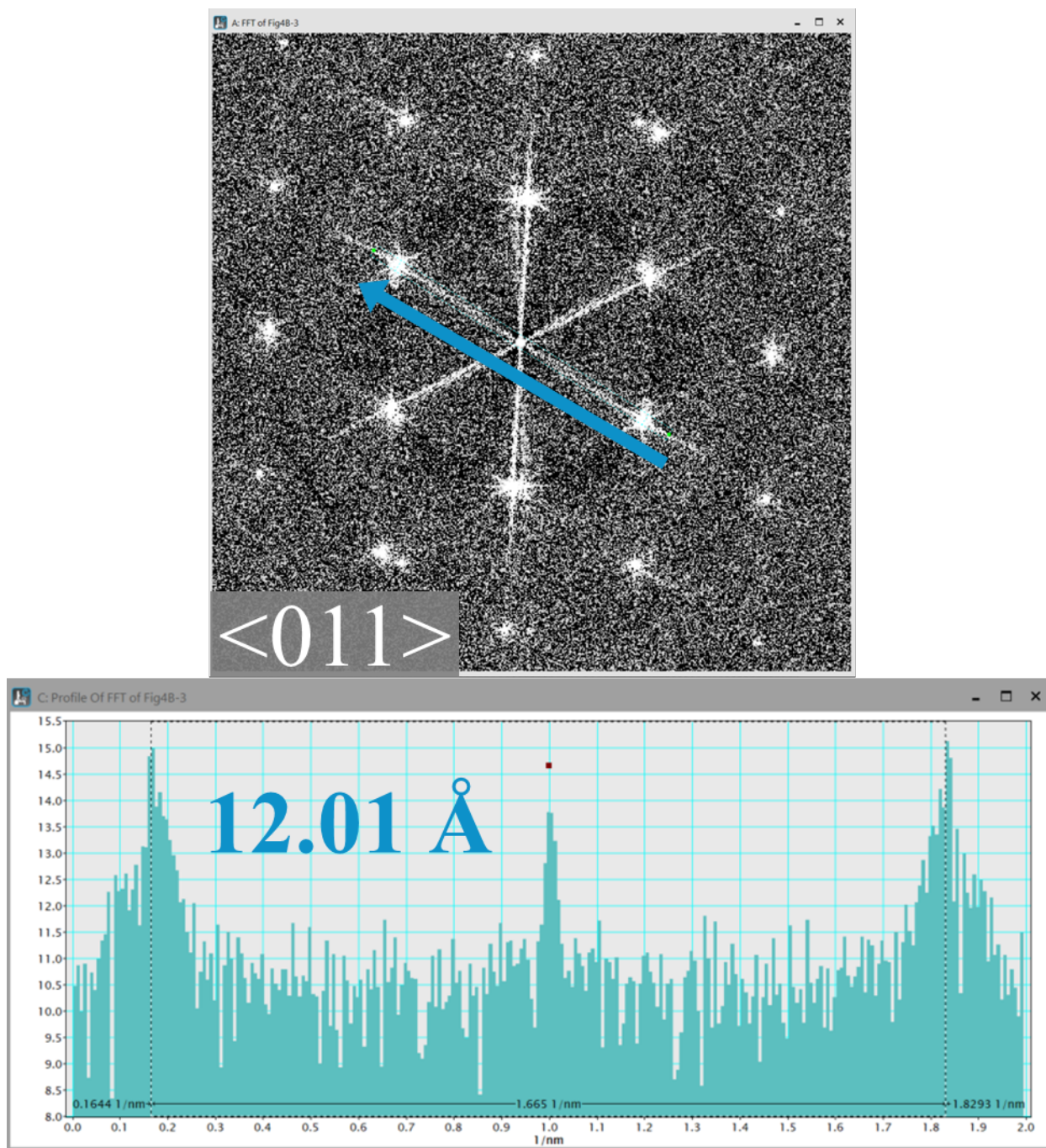


Fig. S10. Empty ZIF-8 $\langle 011 \rangle$ lattice measurement using FFT. Screenshots of FFT (top) and corresponding intensity plot (bottom) of the empty ZIF-8 particle. The $\langle 011 \rangle$ lattice spacing is measured to be 12.01 Å, closely matching the XRD measured value of 12.03 Å. The camera constant was established using a standard Au cross grating TEM grid.

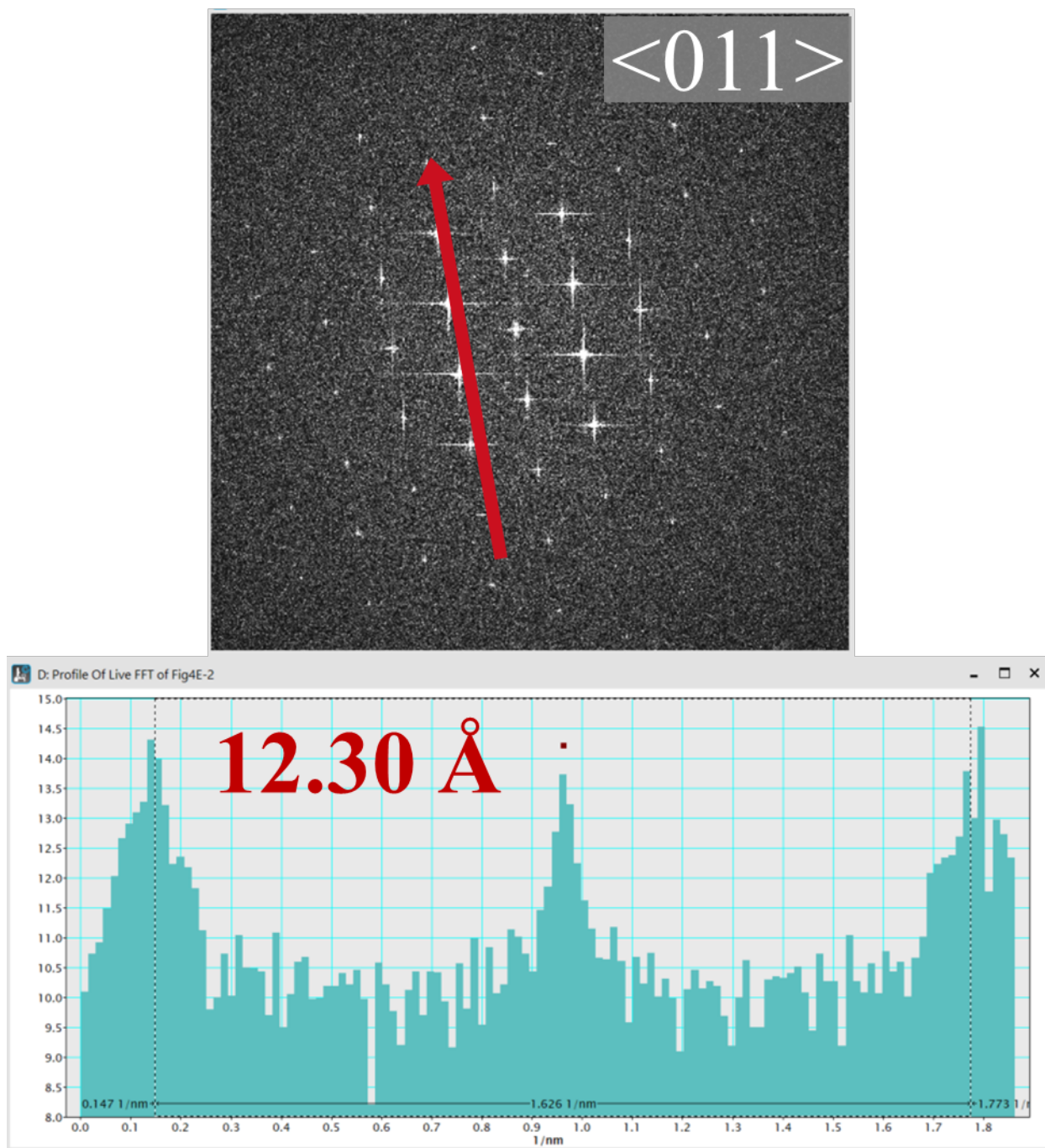


Fig. S11. CO₂-filled ZIF-8 $\langle 011 \rangle$ lattice measurement using FFT. Screenshots of FFT (top) and corresponding intensity plot (bottom) of the CO₂-filled ZIF-8 particle. The $\langle 011 \rangle$ lattice spacing is measured to be 12.30 \AA , an expansion of $\sim 3\%$.

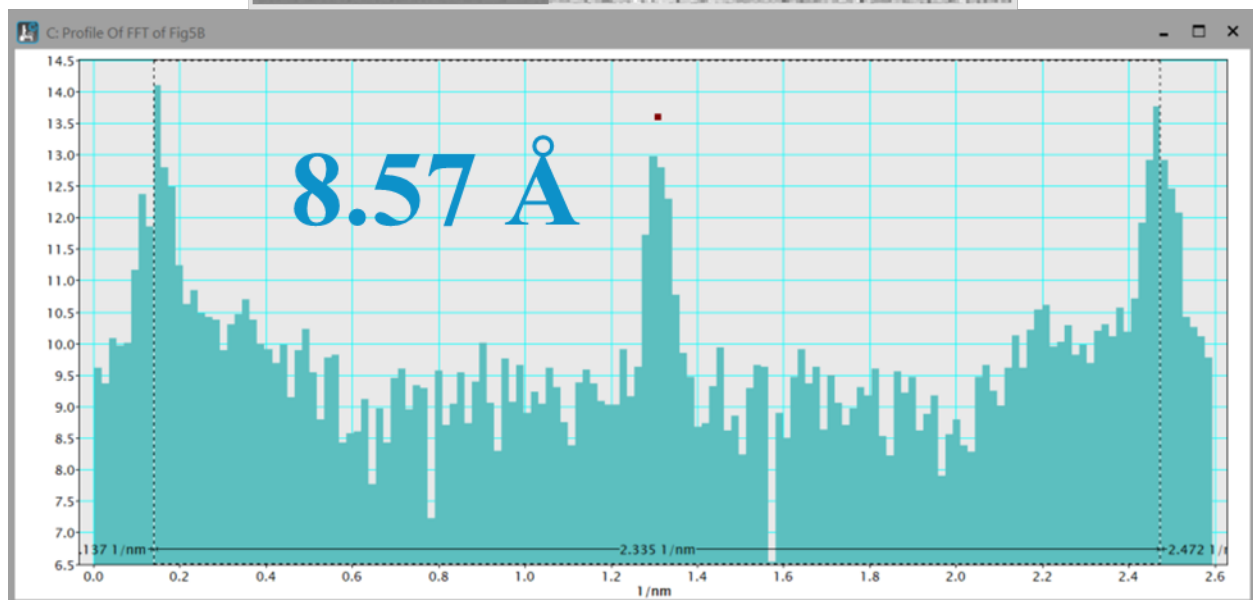
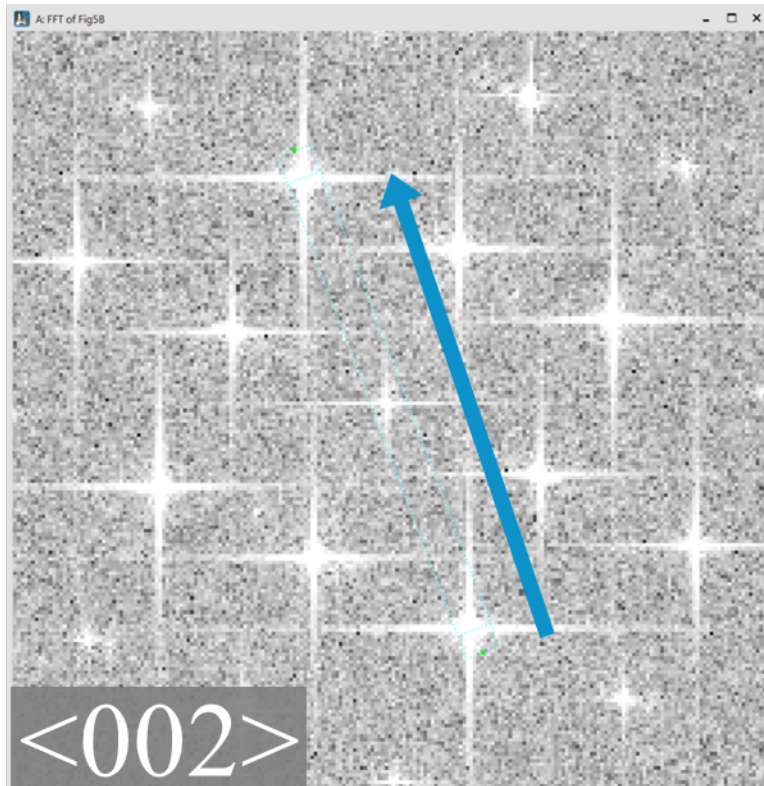


Fig. S12. Empty ZIF-8 <002> lattice measurement using FFT. Screenshots of FFT (top) and corresponding intensity plot (bottom) of the empty ZIF-8 particle. The <002> lattice spacing is measured to be 8.57 Å, close to the XRD measured value of 8.50 Å.

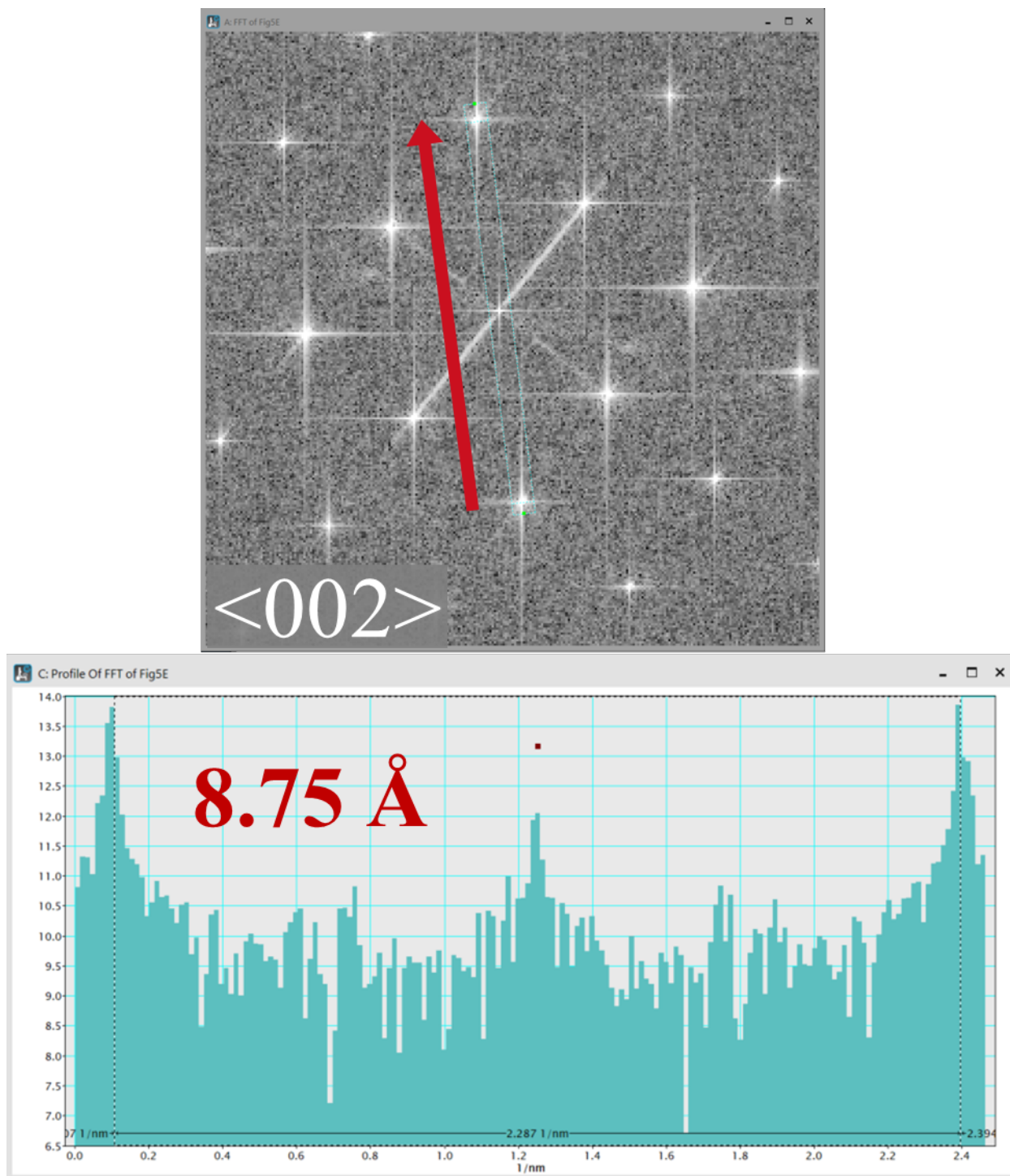


Fig. S13. CO₂-filled ZIF-8 $\langle 002 \rangle$ lattice measurement using FFT. Screenshots of FFT (top) and corresponding intensity plot (bottom) of the CO₂-filled ZIF-8 particle. The $\langle 002 \rangle$ lattice spacing is measured to be 8.75 Å, an expansion of ~3%.

References and Notes

1. Cravillon, J. *et al.* Controlling zeolitic imidazolate framework nano-and microcrystal formation: insight into crystal growth by time-resolved in situ static light scattering. *Chem. Mater.* **23**, 2130–2141 (2011).
2. Zheng, S. Q. *et al.* MotionCor2: anisotropic correction of beam-induced motion for improved cryo-electron microscopy. *Nat. Methods* **14**, 331 (2017).
3. Rohou, A. & Grigorieff, N. CTFFIND4: Fast and accurate defocus estimation from electron micrographs. *J. Struct. Biol.* **192**, 216–221 (2015).
4. Zhang, K. Gctf: Real-time CTF determination and correction. *J. Struct. Biol.* **193**, 1–12 (2016).
5. Crowther, R. A., Henderson, R. & Smith, J. M. MRC image processing programs. *J. Struct. Biol.* **116**, 9–16 (1996).
6. Biyani, N. *et al.* Focus: The interface between data collection and data processing in cryo-EM. *J. Struct. Biol.* **198**, 124–133 (2017).
7. Kilaas, R. Optimal and near-optimal filters in high-resolution electron microscopy. *J. Microsc.* **190**, 45–51 (1998).
8. Rez, D., Rez, P. & Grant, I. Dirac–Fock calculations of X-ray scattering factors and contributions to the mean inner potential for electron scattering. *Acta Crystallogr. Sect. A* **50**, 481–497 (1994).
9. Egerton, R. F., Li, P. & Malac, M. Radiation damage in the TEM and SEM. *Micron* **35**, 399–409 (2004).
10. Egerton, R. F. Mechanisms of radiation damage in beam-sensitive specimens, for TEM accelerating voltages between 10 and 300 kV. *Microsc. Res. Tech.* **75**, 1550–1556 (2012).

11. Vapor Pressure of Carbon Dioxide. *Chemical Engineering and Materials Research Information Center*
12. Bryson III, C. E., Cazcarra, V. & Levenson, L. L. Sublimation rates and vapor pressures of water, carbon dioxide, nitrous oxide, and xenon. *J. Chem. Eng. Data* **19**, 107–110 (1974).